C
S
P

The DOE Center of Excellence for the Synthesis and Processing of Advanced Materials

Member Laboratories: Ames Laboratory, Argonne National Laboratory, Brookhaven National Laboratory, Idaho National Engineering and Environmental Laboratory, University of Illinois Frederick Seitz Materials Research Laboratory, Lawrence Berkeley National Laboratory, Lawrence Livermore National Laboratory, Los Alamos National Laboratory, National Renewable Energy Laboratory, Oak Ridge National Laboratory, Pacific Northwest National Laboratory, and Sandia National Laboratories

Research Briefs
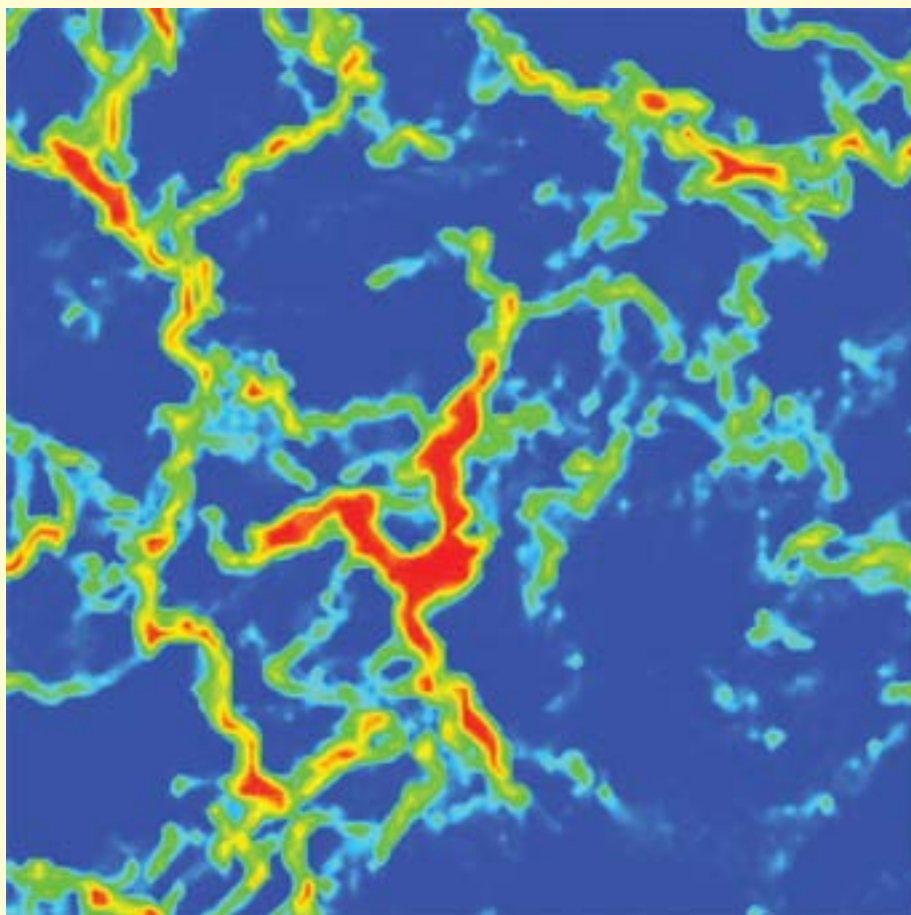
For questions and additional information contact:

George A. Samara
Sandia National Laboratories/NM
Phone: (505) 844-6653
Fax: (505) 844-4045
E-mail: gasamar@sandia.gov

C S P

The DOE **C**enter of Excellence for the
Synthesis and **P**rocessing
of Advanced Materials

Research Briefs

October 2002

Table of Contents

Research Briefs

Table of Contents

Preface

This publication, *Research Briefs*, is designed to inform present and potential customers and partners of the DOE <u>C</u>enter of Excellence for the <u>S</u>ynthesis and <u>P</u>rocessing of Advanced Materials (CSP) about significant advances resulting from Center-coordinated research. The format for *Research Briefs* is an easy-to-read, not highly technical, concise presentation of the accomplishments. Each *Brief* provides a statement of the motivation for the research followed by a description of the accomplishment and its significance.

The Center is a distributed center for promoting coordinated, collaborative research partnerships related to the synthesis and processing of advanced materials. It was established by the Department of Energy's Division of Materials Sciences and Engineering, Office of Basic Energy Sciences and the DOE Laboratories in recognition of the enabling role of materials synthesis and processing to numerous materials fabrication- and manufacturing-intensive technologies. The participants include investigators from 12 DOE national laboratories, universities and the private sector. The Center has a technology perspective provided by a Technology Steering Group.

By bringing together synergistic activities and capabilities in selected focus areas of materials synthesis and processing, the Center's goal is to be a vehicle for providing added value and making impact. The Center is also allowing better coordinated strategic planning by the Division of Materials Sciences and Engineering and the Laboratories and faster response time to special needs and opportunities. Additionally, the Center is serving as a model of R and D integration within the Department of Energy as well as a model of cooperation among the participating institutions.

The overall objective of the Center is,
To enhance the science and engineering of materials synthesis and processing in order to meet the programmatic needs of the Department of Energy and to facilitate the technological exploitation of materials.

Synthesis and processing (S&P) are those essential elements of Materials Science and Engineering (MS&E) that deal with (1) the assembly of atoms or molecules to form materials, (2) the manipulation and control of the structure at all levels from the atomic to the macroscopic scale, and (3) the development of processes to produce materials for specific applications. Clearly, S&P represent a large area of MS&E that spans the range from fundamental research to technology. The goal of basic

research in this area ranges from the creation of new materials and the improvement of the properties of known materials, to the understanding of such phenomena as diffusion, crystal growth, sintering, phase transitions, to the development of novel diagnostic, modeling and processing approaches, etc. On the applied side, the goal of S&P is to translate scientific results into useful materials by developing processes capable of producing high quality, cost-effective products.

The technical emphasis of the Center is on a number of focused multilaboratory projects which draw on the complementary strengths of the member institutions in their ongoing research programs. These projects were selected on the basis of the following criteria:

- scientific excellence

- clear relationship to energy technologies

- involvement of several laboratories

- existing or potential partnerships with DOE Technologies-funded programs

- existing or potential "in-kind" partnerships with industry

Each Project is coordinated by a knowledgeable representative from one of the participating laboratories. The Projects covered in this issue of *Research Briefs* and their Coordinators are listed in the accompanying table (p. 7). A few selected accomplishments from each of the Projects are presented. An Executive Summary provides highlights of these accomplishments organized by Project. Readers are encouraged to contact any of the Coordinators for information about the Center and its accomplishments.

One of the projects listed in the table on page 7, namely, *Design and Synthesis of Ultrahigh-Temperature Intermetallics,* graduated at the end of FY2002. It has been replaced by the new Project, *Experimental and Computational Lubrication at the Nanoscale* which is scheduled for FY2003 start. Center Projects are graducted after achieving their objectives, but no later than five years after start.

George A. Samara
October 2002

The Center's Member Laboratories

The member laboratories of the Center are:

- Ames Laboratory (Ames)
- Argonne National Laboratory (ANL)
- Brookhaven National Laboratory (BNL)
- Idaho National Engineering and Environmental Laboratory (INEEL)
- University of Illinois Frederick Seitz Materials Research Laboratory (UI/MRL)
- Lawrence Berkeley National Laboratory (LBNL)
- Lawrence Livermore National Laboratory (LLNL)
- Los Alamos National Laboratory (LANL)
- National Renewable Energy Laboratory (NREL)
- Oak Ridge National Laboratory (ORNL)
- Pacific Northwest National Laboratory (PNNL)
- Sandia National Laboratories (SNL)

Membership of the Technology Steering Group

Member	Affiliation
Prof. L. Eric Cross	Pennsylvania State University
Dr. David W. Johnson, Jr.	Agere Systems
Dr. Hylan B. Lyon	Marlow Industries
Dean Paul S. Peercy	University of Wisconsin
Dr. Charles Sorrell	DOE/Energy Efficiency & Renewable Energy
Dr. John Stringer	Electric Power Research Institute (EPRI)
Dr. Arthur Yang	Arthur Yang Industrial Science and Technology Network, Inc.
Dr. Udaya Rao	DOE/Fossil Energy
Dr. Christian Mailhot	DOE/Defense Programs; Lawrence Livermore National Laboratory

Center Projects Covered In This Issue Of *Research Briefs* and Their Coordinators

Project	Coordinator(s)
Nanocomposite Magnets	Samuel D. Bader (ANL) Phone: (630) 252-4960 E-mail: bader@anl.gov
Smart Structures Based on Electroactive Polymers	Gregory J. Exarhos (PNNL) Phone: (509) 375-2440 E-mail: greg.exarhos@pnl.gov
Ultrahigh-Temperature Intermetallics	Roddie R. Judkins (ORNL) Phone: (865) 574-4572 E-mail: judkinsrr@ornl.gov and R. Bruce Thompson (Ames) Phone: (515) 294-8152 E-mail: thompsonrb@cnde.iastate.edu
Nanoscale Phenomena in Perovskite Thin Films	Orlando Auciello (ANL) Phone: (630) 252-1685 E-mail: auciello@anl.gov and Duane Dimos (SNL/NM) Phone: (505) 844-6385 E-mail: dbdimos@sandia.gov
The Science of Localized Corrosion	Kevin Zavadil (SNL/NM) Phone: (505) 845-8442 E-mail: krzavad@sandia.gov
Controlled Defect Structures in Rare-Earth-Ba-Cu-O Cuprate Superconductors	David O. Welch (BNL) Phone: (631) 344-3517 E-mail: dwelch@bnl.gov
Carbon-Based Nanostructured Materials	John Carlisle (ANL) Phone: (630) 252-4960 E-mail: carlisle@anl.gov and Thomas Friedmann (SNL/NM) Phone: (505) 844-6684 E-mail: tafried@sandia.gov
Granular Flow and Kinetics	David Hoffman (Ames) Phone: (515) 294-9649 E-mail: hoffman@ameslab.gov
Overall Center Coordinator	George A. Samara (SNL/NM) Phone: (505) 844-6653 E-mail: gasamar@sandia.gov

Executive Summary

The *Research Briefs* presented in this publication are intended to inform the Center's present and potential customers and partners about significant advances resulting from Center-coordinated research. Selected accomplishments from each of the eight Center focused projects are presented. This Executive Summary states the overall objective of each project followed by highlights of the accomplishments presented later in more detail.

Nanocomposite Magnets

Objective — *Develop improved understanding of magnetic properties and improved magnetic materials using nanoscale mixtures of hard magnets, soft magnets and non-magnetic materials.*

Highlights

- Resonant soft-x-ray scattering measurements yielded the first direct measurement of magnetic correlation length in complex Co-based polycrystalline ferromagnetic thin films as well as the evolution of this correlation length with composition. Control over the strength and length of correlations among polycrystalline grains can lead to significant gains in magnetic recording density and other applications of magnetic thin films. (p. 14)

- It has been shown that ion-beam processing can be used to tailor the nature of the interfaces, and thus the magnetic properties of exchange-spring magnets. Additionally, analytical modeling and kinetic Monte Carlo simulations have shown that it should be possible to induce self-organization of thin film microstructure into nanopatterns by irradiation. (p. 16)

- Nanomagnetic composites of MnAu + Fe and MnAu + (Fe, Co) are being investigated as possible alternatives to rare-earth intermetallic compounds such as $RE_2Fe_{14}B$ and $RECo_5$ for strong permanent magnets. Early results have given evidence for the sought-after interaction between the ferro-and antiferromagnetic phases in these materials as well as for a large increase the coercivity resulting from structural refinement via high-energy ball milling. (p. 18)

Smart Materials Based on Electroactive Polymers

Objective
Develop a framework for the rational design of self-assembled nanostructured block copolymers that offer significant advantages over conventional materials for the active regulation of transport phenomena.

Highlights

- A synthetic approach has been developed that allows chemical binding of poly (N-isopropylacrylamide) (PNIPAM) as a dense monolayer to a hydroxylated silica surface. The bound PNIPAM is shown to reversibly adsorb and release protein via a (near body) temperature-induced hydrophobic-to-hydrophilic phase transformation. (p. 20)

- Diblock copolymers have been developed that spontaneously organize into molecular wires in the presence of certain solvents. Under the proper processing conditions, the hydrophobic blocks form cladding around the more hydrophobic regions allowing the formation of conducting wire surrounded by insulated cladding. (p. 22)

- Large arrays of uniform and oriented nanowires of conducting polymers on a variety of substrates have been prepared by controlled nucleation and growth using a step-wise electrochemical deposition process. The process was demonstrated for molecularly-aligned polyaniline molecules assembled into a uniform nanowire array without the use of a templating agent. (p. 24)

Ultrahigh-Temperature Intermetallics

Objective
Generate the knowledge required to establish a scientific basis for the design and processing of transition-metal silicides and materials based on silicides for structural applications at temperatures of 1400°C and above.

Highlights

- It has been shown that Mo-Si-B silicide alloys can be processed with higher fracture toughness and more fatigue resistance than monolithic $MoSi_2$ and its alloys. Additionally, their crack-growth resistance, in both fracture and fatigue, progressively increases with increasing temperature up to 1300° C. (p. 26)

- The high temperature strength of Mo-Si-B alloys has been shown to depend strongly on the topology and scale of the alloy's microstructure. For comparable compositions, the creep strength can be varied by as much as a factor of two by manipulating the microstructure and its scale. (p. 28)

- It has been shown that a protective scale forms on Mo-Si-B alloys during isothermal oxidation that significantly reduces oxygen transport and the formation of Mo and MoO_2 precipitates at the scale/alloy interface. These borosilicate scales as well as sulfide scales formed during sulfidation experiments may greatly improve oxidation and corrosion resistance. (p. 30)

Nanoscale Phenomena in Perovskite Thin Films

Objective

Develop the scientific basis for controlling nucleation, growth and strain in fer-roelectric perovskite thin films.

Highlights

- *In-situ* synchrotron x-ray scattering studies have allowed determination of the optiumum conditions for MOCVD growth of $PbTiO_3$ thin films and demonstrated that it is possible to achieve layer-by-layer and step-flow growth during MOCVD of multicomponent oxides. (p. 32)

- *In-situ* time-of flight ion scattering and recoil spectrometry and spectroscopic ellipsometry have been combined to provide mass and structure analysis as well as growth dynamics and optical properties of as-deposited thin layers of complex oxide thin films, thereby providing critical insight into interface formation and evolution. (p. 34)

- Novel techniques have been developed to fabricate micro-to-nano-scale capacitor structures of thin film PZT. Measurements on capacitors that differ by a factor of 100 in diameter have given new insights into the piezoelectric response of small structures. (p. 36)

- Combined surface and interface thermodynamics, in-situ XPS characterization of band-edge alignment and first-principles energy calculations have shown that an interface phase (not simply a bulk termination junction) defines the electrostatic boundary condition of oxide/semiconductor interfaces. (p. 38)

The Science of Localized Corrosion

Objective

Advance the fundamental understanding of the mechanisms leading to the initiation, propagation and cessation of localized corrosion of aluminum and its alloys to permit accurate life predictions and intelligent designs.

Highlights

- Correlation among microstructure, topography and conductivity for a plasma-formed oxide on an Al thin film was demonstrated using TEM, contact force microscopy and current-sensing force microscopy. This correlation along with electrochemical measurements have shown that local variations in oxide conductivity can generate instability and lower the threshold for pitting corrosion. (p. 40)

- A 3-D Kinetic Monte Carlo model developed to describe pitting corrosion is generating important chemical and physical information including local chemistry, shape factor, and instantaneous propagation velocity. (p. 42)

- The effects of Cu on Al alloy corrosion both in the presence and in the absence of a passive film were investigated. In the absence of a film, Cu appears to promote localized corrosion through selective oxidation of the Al, whereas in the presence of a film Cu seems to inhibit corrosion. (p. 44)

Controlled Defect Structures in Rare-Earth-Ba-Cu-O Cuprate Superconductors

Objective

Provide an integrated scientific understanding of lattice defects and their nanoscale structure in the "123" rare-earth cuprates and related compounds, their dependence on the various methods of synthesis, and their relationship to the resulting superconducting properties.

Highlights

- X-ray diffraction, cross-sectional TEM and x-ray spectral analysis have identified the existence of nanocracks in YBCO films grown by two different processes on $SrTiO_3$ buffers, which are in turn grown on Ni (100) substrates, and attributed these cracks to NiO formation during growth. Pathways exist for solving this critical materials issue. (p. 46)

- Large critical current density (J_c) values as high as 250 kA /cm^2 at 77K are observed for YBCO films grown on Inclined-Substrate-Deposited MgO coated-conductor templates with $LaMnO_3$ buffer layers. The results suggest a method to produce cost-effective, long-length superconductors. (p. 48)

- Experimental and modeling results have shown that oxygen in the grain boundaries, strain and oxygen disorder have strong influences on the critical current density of YBCO. Systematic improvements in J_c with increasing oxygen content that extends beyond the optimal doping (i.e., maxiumum T_c) of the grains have been demonstrated. (p. 50)

Carbon-Based Nanostructured Materials

Objective

Advance the science and technology of carbon-based materials that will lead to the development of new generations of MEMS and NMES devices.

Highlights

- *In-situ* nanoindentation of amorphous diamond thin films in a TEM have shown the robustness of these films on Si substrates. The results indicate that micromachined devices coated with amorphous diamond can be expected to retain their superior mechanical and chemical properties even after the application of large and highly localized stress. (p. 52)

- Density-functional-based tight binding calculations have defined the potential energy surface for the addition of C_2 to a nonhydrogenated dimer site on the (100) diamond surface. The deposition barriers are found to be higher and the pathways more complex than for deposition on the (110) surface - a finding that should help understand the observed growth of small grain sizes. (p. 54)

- NMR and annealing studies on completely enriched (99%) ^{13}C amorphous diamond films have shed much light on the nature of the bonding and mechanism for stress relaxation in these films. The relaxation is due to the ordering of the sp^2 and sp^3 bonding configurations. (p. 56)

Granular Flow and Kinetics

Objective

Develop constitutive relationships for the dynamic response of granular materials capturing the breadth of granular kinetics and flows in fundamental ways.

Highlights

- Exact analytical solutions in the kinetic theory of granular gases have provided important insights into the physics of these materials and revealed fundamental differences between granular and molecular gases. Complementary simulations have resolved outstanding issues concerning clustering and velocity statistics in freely evolving granular gases. (p. 58)

- Using a highly parallel molecular dynamics code, large systems of granular particles have been modeled yielding precise information about behavior in the bulk of a granular system, behavior that cannot be obtained experimentally. These simulations can give valuable guidance for continuum models and the development of constitutive relations. (p. 60)

- Studies of the particle velocity distributions in electrostatically-driven granular media have shown that short-range forces contribute to the observed non-Gaussian distributions, a finding that may have relevance to dusty plasmas and charged colloids. Electrostatic driving makes use of bulk forces and allows control of the ratio between long-range electric forces and short-range collisions by changing the amplitude and frequency of the applied electric field. (p. 62)

Research Briefs

Resolving Nanometer Scale Magnetic Correlation Lengths in Complex Alloys

J. B. Kortright, *Lawrence Berkley National Laboratory*
O. Hellwig, D. T. Marguiles, B. Lengsfield, *and* **E. E. Fullerton,** *IBM Almaden Research Center*

Motivation—Magnetic recording alloy films consist of chemically segregated, poly-crystalline grains whose centers are ferromagnetic with in-plane anisotropy and whose boundaries are nominally nonmagnetic. This chemically and magnetically heterogeneous microstructure has evolved through several generations via an increasingly complex set of alloys from CoCr to CoPtCr to CoPtCrB. The additives Cr and B are known to segregate to and produce nonmagnetic grain boundary phases that were believed to reduce exchange coupling between adjacent grains, thereby enabling sharper bit transitions and higher recording density. Chemical heterogeneity associated with these films is resolved using high-resolution TEM as seen in Figure 1. It has remained difficult, however, to directly measure the magnetic correlation length giving the distance over which grain-to-grain magnetism is correlated.

Accomplishment—We have used resonant soft x-ray scattering to make the first direct measurements of magnetic correlation lengths in complex Co alloys and to follow the evolution of this correlation length with composition. Three films were grown on a common buffer layer structure similar to that presently in use. The x-ray scattering used synchrotron radiation at the Advanced Light Source at LBNL.

Scattering data for the three alloy films and their common underlayer structure are shown in Figure 2. These data were collected at two different x-ray energies near the Cr and Co L_3 core resonances. Also shown for the alloy samples is the difference between the Co and Cr edge data. The Cr-edge data have a peak at $q \cong 0.07$ Å^{-1} for all samples resulting from interference between neighboring scattering centers separated by $2\pi/q \cong 100$ Å. These Cr resonant peaks measure the average grain diameter as seen in Figure 1.

The Co-edge scattering is expected to arise from both magnetic and chemical correlations. These data show the same $q \cong 0.07$ Å^{-1} peak observed in the Cr-edge data, as well as additional scattering at much lower q values that must result from magnetic scattering between regions having different magnetic orientation that are much larger than the chemical grain size. The difference of the Co and Cr resonant scans results from Co magnetic-magnetic correlations and magnetic-charge interference, with the former dominating the low-q peak and the latter contributing progressively to increasing q. The low-q peak is thus a measure of the magnetic correlation length in these films.

In the progression of alloy compositions it is seen that the magnetic correlation length remains unchanged between CoCr and CoPtCr, and moves much closer to the grain size peak for the boron-containing sample. Boron addition is thus quite effective in reducing magnetic correlation lengths in these recording media alloys.

Significance—Direct measurement of magnetic correlation lengths enables systematic studies of the effects composition, growth, and processing that will improve our understanding of these and other nanostructured magnetic materials. Control over the strength and length of correlations among polycrystalline grains can lead to gains in recording density and other applications of magnetic thin films.

Contact: J. B. Kortright, Lawrence Berkeley National Laboratory
        Phone: (510) 486-5960, Fax: (510) 486-5530, E-mail: jbkortright@lbl.gov
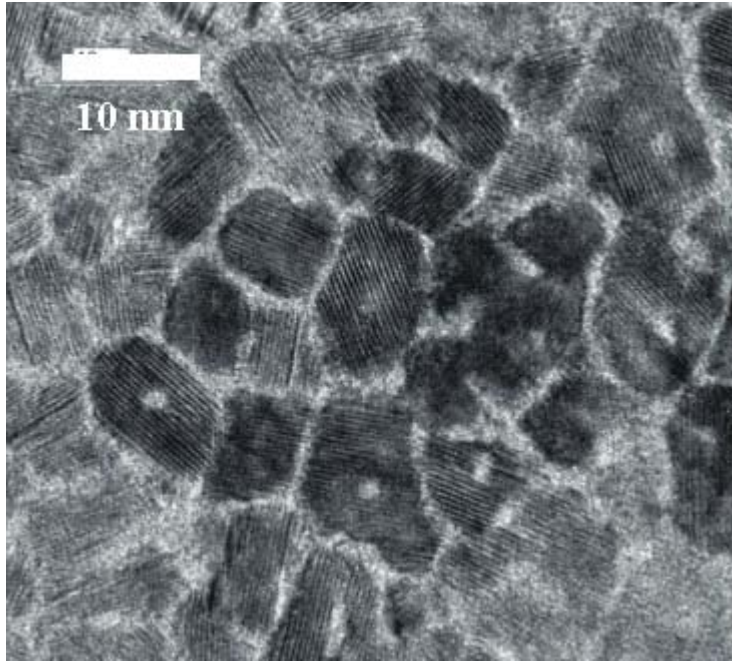
Figure 1. This high-resolution transmission electron microscope (TEM) image shows the polycrystalline grain structure in a CoPtCrB recording media film. Routine analytical techniques can reveal that Cr and B segregate to the grain boundary areas that are lighter in color and believed to be non-magnetic. The darker grain centers are rich in Co and Pt and are magnetic. Until now it has remained difficult to measure the magnetic correlation length that gives the distance over which the grain-to-grain magnetization is strongly coupled. Short magnetic correlation lengths are desired for recording media alloys, since this length sets a limit on how sharp the magnetic transition between memory bits can be. (Photo courtesy Kai Tang, IBM).

Figure 2. Resonant x-ray scattering from the underlayer structure without media layer (a) and from CoCr (b), CoPtCr(c), and CoPtCrB (d) media measured at the Co and Cr L_3 lines as indicated. The inset shows the scattering geometry and media layer with magnetic grains (diameter D) with the in-plane magnetization direction represented by the arrows and nonmagnetic grain boundaries. The open diamonds are the difference between the Co- and Cr-edge data (scaled to match at high q). The dashed line in (b) is the non-resonant scattering measured 10 eV below the Co edge. Intensity peaks result from interference between the scattering from well-defined neighboring scattering centers. The high q peaks in the Cr-edge data give the average chemical grain size of about 100 Å. The low q peaks in the difference data approximate the magnetic-magnetic interference and show how the magnetic correlation length changes with alloy composition.
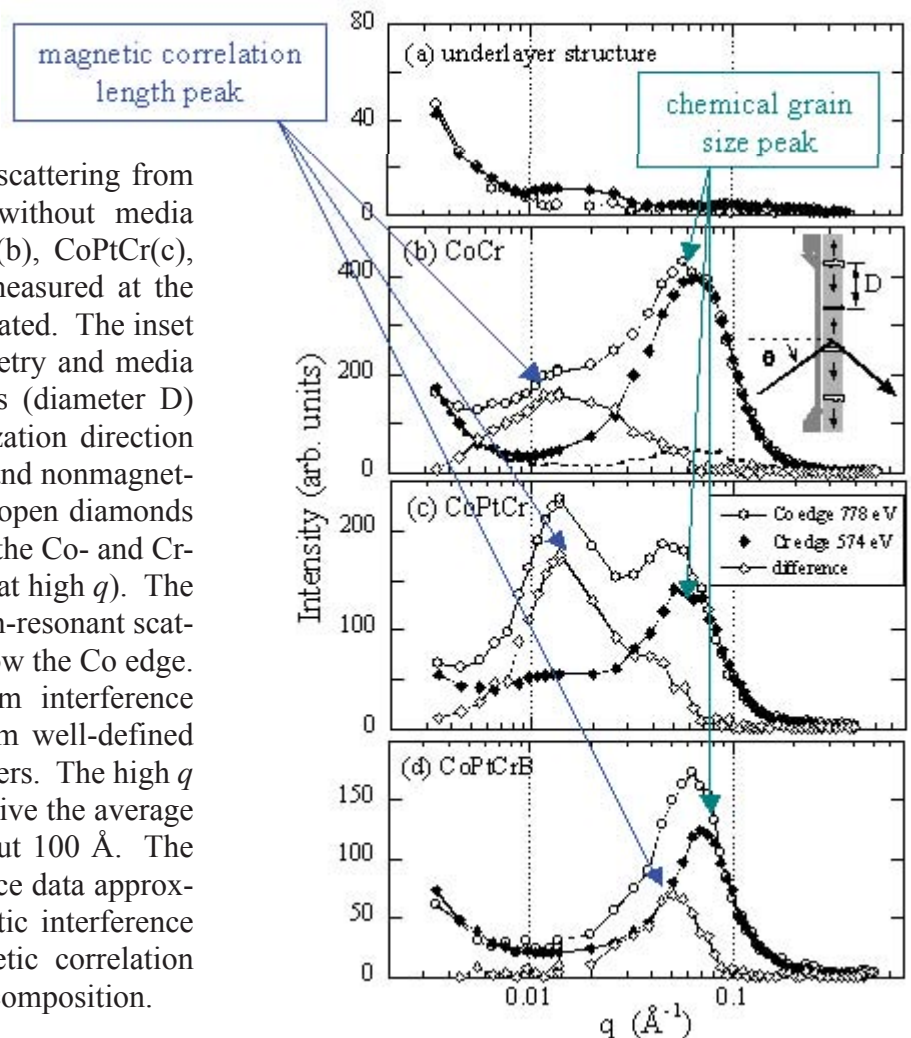
Tailoring Interfacial Properties of Exchange-Spring Permanent Magnets

R. S. Averback, P. Bellon and ***M. B. Salamon,*** *University of Illinois at Urbana-Champaign*
J. S. Jiang and ***S. D. Bader,*** *Argonne National Laboratory*

Motivation—Multilayer exchange spring permanent magnets consist of a stacking of interfacial exchange coupled hard and soft magnetic nanolayers that combine the high magnetization of the soft phase with the high anisotropy of the hard phase to attain a high energy product. Interfaces between the two magnetic phases play a determinant role in the static and dynamic properties of these nanocomposite magnets. Interface roughness should be kept to a minimum to ensure a tight control of the thickness of these nanolayers, whereas recent work at ANL establishes that chemical mixing is beneficial to prevent the catastrophic collapse of magnetic induction during demagnetization. The present collaborative work is aimed at tailoring these interface properties by ion-beam processing, and at applying this process to exchange spring magnets. In addition, we investigate the possibility of synthesizing three-dimensional nanocomposite exchange-spring magnets through an irradiation-induced self-organization reaction.

Accomplishment—In order to study the fundamentals of the evolution of interface roughness during ion-beam processing, we have first selected the easier case of a free surface, for which the roughness can be directly measured using atomic force microscopy (AFM). As shown in Fig. 1, ion irradiation at moderate doses can be used to reduce below 0.5 nm the surface roughness of an amorphous film (Fig, 1). We have recently extended the study to the case of Ni/Ag interfaces, and we have observed a similar roughness evolution during irradiation.

In parallel to this fundamental study, Sm-Co/Fe bilayer exchange spring magnets grown at ANL have been subjected to ion beam processing. Figure 2 indicates that strong irradiation conditions should be avoided as they result in the damage of the hard magnetic compound, leading to a reduction of its coercive field.

Finally, we have used analytical modeling and atomistic computer simulations (kinetic Monte Carlo) to investigate the possible self-organization of thin film microstructure into nanocomposites suitable for exchange spring magnets. Our past results indicated that such a self-organization could take place in alloy systems made of immiscible elements (e.g., Cu-Ag). We have extended these results to the case of alloys containing ordered phases, as nearly all alloy systems considered for exchange spring magnets contain an ordered phase (e.g., Co_5Sm, FePt, CoPt). Figure 3 indicates that it is indeed possible to induce a self-organization of the film into nanopatterns (state P), provided that the irradiation parameters are properly chosen. We are currently testing these predictions on Fe-Pt thin films.

Significance—High-performance permanent magnets may afford the advantages of increased efficiency in energy production and energy systems. Understanding the microstructure-properties relationships is necessary in order to optimize exchange-spring permanent magnets. Our first results show that ion-beam processing makes it possible to tailor the nature of the interfaces, and thus the magnetic response of these exchange-spring magnets.

Contact: R. S. Averback, University of Illinois at Urbana-Champaign
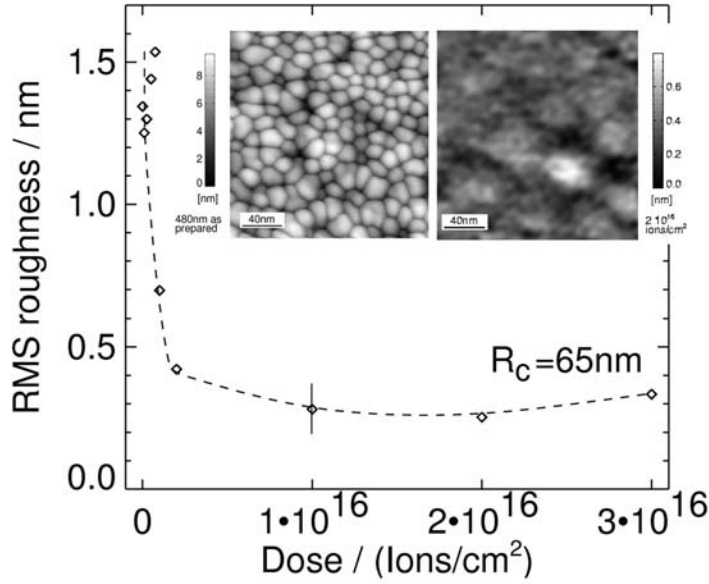Phone: (217) 333-4302, Fax: (217) 244-2278, E-mail: averback@uiuc.edu

Figure 1. Evolution with radiation dose of surface roughness and lateral structure size R_C of a 480 nm amorphous $Zr_{65}Al_{7.5}Cu_{27.5}$ film irradiated with 1.8 MeV Kr+ ions. AFM surface topographs (insets) illustrate the smoothening of the initial surface (left) after irradiation to a dose of $2x10^{16}$ ions/cm^2 (right).
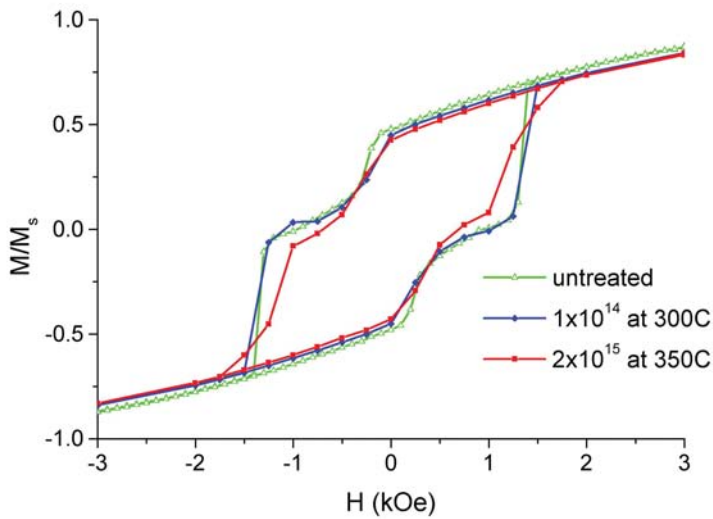

Figure 2. Hysteresis loops of a Sm-Co(80 nm)/Fe(200 nm) bilayer exchange spring magnet, in the as-grown state and after 620 keV He irradiation at 300°C and 350°C, with doses ranging from $1x10^{14}$ ions/cm^2 to $2x10^{15}$ ions/cm^2. Irradiation at the highest temperature and dose has damaged the hard magnetic phase, resulting in a decrease of the coercitive field.
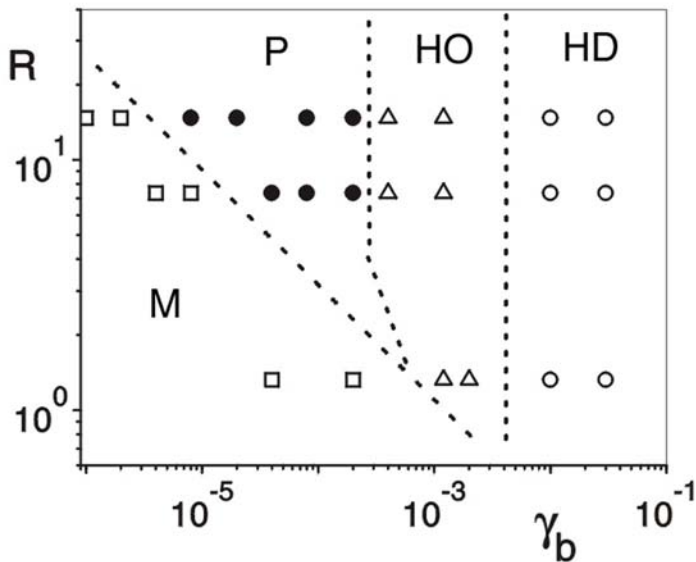

Figure 3. Dynamical phase diagram predicted from atomistic computer simulations, indicating the microstructure stabilized by irradiation for an initially two-phase material, comprised of an ordered phase and a disordered phase coexisting at a macroscopic scale (phase M). As a function of the relative irradiation intensity (γ_b), and the range of atomic mixing produced by irradiation (R), irradiation can stabilize a homogeneous disordered state (HD), a homogeneous ordered state (HO) or a patterned state (P) where the ordered and disordered phases coexist at the nanometer scale. For an appropriate alloy this self-organized patterning can be used to synthesize exchange spring-magnets at a controlled scale by ion-beam processing.

17

Towards Rare-Earth-Free High Energy-Product Magnets

L. H. Lewis and *C.L. Harland,* Brookhaven National Laboratory
M. J. Kramer and *R. W. McCallum,* Ames Laboratory
D. J. Branagan, Idaho National Engineering and Environmental Laboratory

Motivation—Permanent magnetic materials underlie the operation of motors of every kind, perform crucial tasks in computers, and provide functionality in devices ranging from personal stereos through hearing aids to surgical tools. Today's most powerful permanent magnets for specialized application are based on intermetallic compounds such as $RE_2Fe_{14}B$ and $RECo_5$, where RE is a rare-earth element such as Nd, Pr or Sm. The rare-earth elements provide strong magnetic coupling in the crystal structure that affords the material with a very high resistance to magnetic reversal. The magnetic benefits conveyed by the rare-earth elements in these magnetic compounds are counterbalanced by their drawbacks: rare-earth elements are expensive, heavy and very susceptible to corrosion, plus the intermetallic compounds that incorporate these elements are brittle and difficult to form into required shapes. The need for a new paradigm for the microstructural design of permanent magnetic materials is long overdue.

Accomplishment—It is anticipated that a nanocomposite material with robust coupling between antiferromagnetic nanoparticles and a high-moment ferromagnetic matrix has the potential to produce a thermally-stable, inexpensive, lightweight permanent magnet. To this end, basic scientific synthesis and characterization studies are underway on melt-spun ribbons of the composite alloy (AuMn + Co) or (AuMn + Fe). These materials combinations were chosen because of the low solubility of antiferromagnetic AuMn in ferromagnetic Co or Fe, and because the $Au_{1-x}Mn_x$ alloy has a Néel temperature T_N that shows a strong dependence with stoichiometry. The latter feature allows the blocking temperature T_B of the nanocomposite alloy, and the associated collective magnetic properties, to be monitored in a controllable way. Initial experiments using rapid solidification revealed the existence of a range of liquid immiscibility between the Fe and/or Co and the anti-ferromagnetic AuMn (Figure 1). While rapid solidification cannot be used to produce nanocomposites, mechanical milling was shown to be effective in reducing the length scale of the phase separation. Cold-rolling of cast alloys produced a laminar microstructure with a large increase in interfacial contact area between the ferro and antiferromagnetic phases (Figure 2). Studies are ongoing to investigate how grain boundaries, role orientation and the chemical order/disorder of the antiferromagnetic phase may dictate magnetic properties.

Significance—Preliminary results of studies performed on nanocomposite MnAu + Fe and MnAu + (Fe,Co) show modest promise in the attainment of a rare-earth-free permanent magnetic material. A small asymmetric shift in the measured hysteresis loops is confirmed at low temperatures in melt-spun alloys, signaling the magnetic interaction between the ferromagnetic and antiferromagnetic phases. A five-fold increase in the coercivity and hysteresis loop shift in the alloys is noted after structural refinement via high-energy ball milling. However, it is apparent that the optimal nanocomposite structure has yet to be achieved, and further processing studies are underway.

Contact: Laura H. Lewis, Brookhaven National Laboratory
Phone: (631) 344-2861, Fax: (631) 344-4071, E-mail: lhlewis@bnl.gov
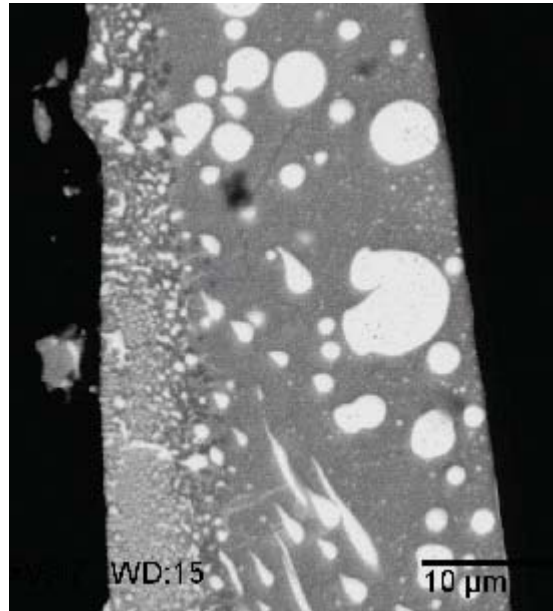
Figure 1. SEM micrograph of cross-section of melt spun ribbon of nominal composition $(Fe_{65}Co_{35})_{85}(AuMn)_{15}$. Bright regions are AuMn phase.
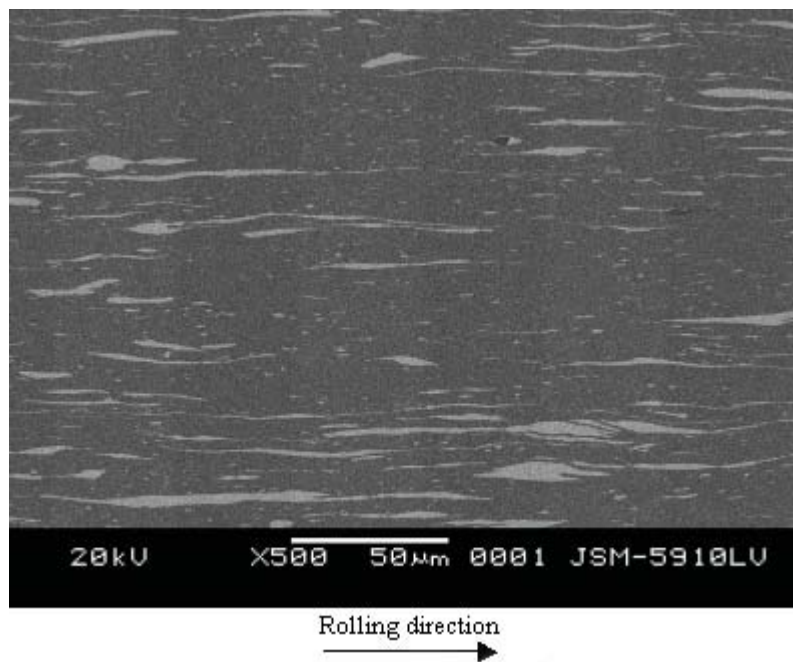

Figure 2. SEM micrograph of rolled $Fe_{95}(AuMn)_5$.

Surface Template Approach for Reactive Monolayers

B.C. Bunker, D.L. Huber, and J. Liu, Sandia National Laboratories, NM
J-H. Chang, and Y. Shin, Pacific Northwest National Laboratory

Motivation—The affinity of a protein molecule to a surface is dependent upon the conformation of that protein which is controlled by the attendant hydrogen bonding both within the protein and to the surface, and the density of protein surface adsorption sites. Solution chemistry, attendant hydrophobicity, and ambient temperature all are known to affect localized hydrogen bond interactions in these systems. Based upon these considerations, surfaces can be engineered to reversibly adsorb and release protein molecules. Potential technology innovations relate to microfluidic platforms where reversible absorption and release of protein molecules from a surface can be used for sensing and drug delivery applications.

Accomplishment—An *in situ* free radical polymerization approach was used to bind a dense monolayer of poly(N-isopropylacrylamide) (PNIPAM) to a silica surface. The chemistry utilized was based on silane coupling agents, maximizing versatility by allowing the functionalization of a number of hydroxide-coated surfaces common in microfabricated devices. The PNIPAM functionalized surface becomes responsive to its ambient environment, as the bound polymer undergoes a reversible expansion-collapse transformation near body temperature. Going from a hydrophilic state (protein release) at low temperature, to a hydrophobic state (protein adsorption) at high temperature (figure 1). It also was found that a rinse of the surface with a non-polar solvent would induce a hydrophobic surface state while

a water rinse of the surface would lead to a hydrophilic surface. The latter effect can be accentuated through the use a mixed monolayer consisting of PNIPAM and polystyrene. In this system alternate exposure to toluene and water causes a change in contact angle of 80°. Since proteins tend to preferentially adsorb on hydrophobic surfaces (as demonstrated in figure 2), these observations can be used to functionalize a microchip that has applications for reversible adsorption or delivery of protein molecules. Reversibility is a major concern in switchable surface, and figure 3 shows evidence of the low hysteresis in the advancing contact angle as a function of temperature. The reversibility of the underlying hydrophilic-hydrophobic transition gives these PNIPAM functionalized surfaces very good reversible protein adsorption properties.

Significance—A synthetic approach has been developed that allows chemical binding of PNIPAM as a dense monolayer to a hydroxylated surface. The bound system shows activity to reversible protein adsorption as a function of temperature and/or ambient solvent hydrophobicity. The adsorption and subsequent desorption of intact globular proteins (eg. myoglobin, serum albumin, and cytochrome C) from a PNIPAM functionalized surface has been demonstrated. It appears likely that this technology can be used to functionalize hierarchically complex substrates. This approach could be used to impart protein specificity into the material.
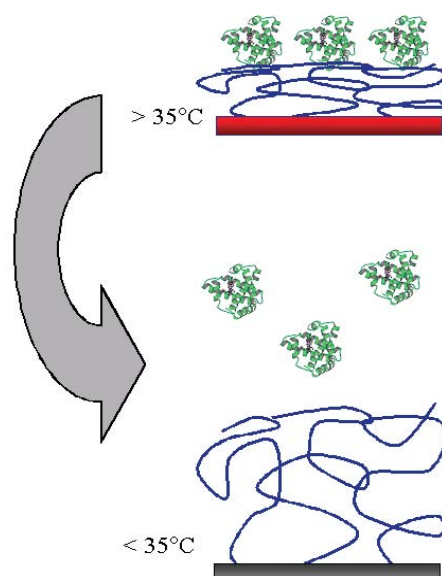
Contact: Bruce Bunker, Sandia National Laboratories, NM
Phone: (505) 284-6892, Fax: (505) 844-5470, E-mail: bcbunke@sandia.gov

Figure 1. A schematic representation of a protein mono-
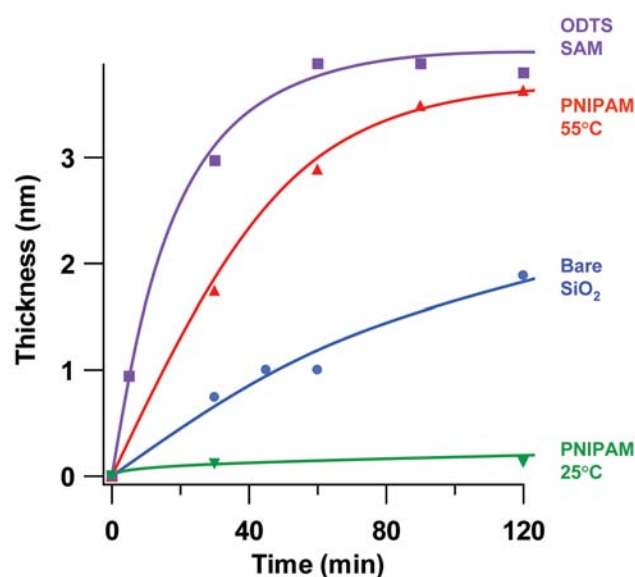layer desorbing from a PNIPAM functionalized surface.

Figure 2. Ellipsometry results showing the adsorption of human serum albumin from a 0.5 mg/ml solution (0.05 M, pH 6 phosphate buffer) on PNIPAM-coated surfaces relative to other model surfaces. Adsorption is negligible on PNIPAM below the transition temperature, while a protein monolayer eventually forms on PNIPAM above the transition temperature.
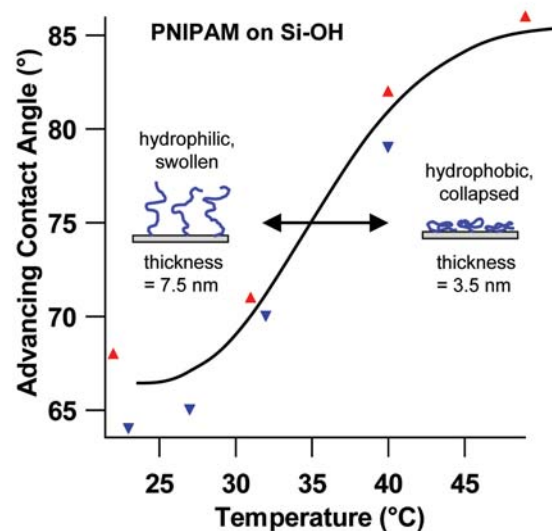

Figure 3. Water contact angle measurements obtained on a PNIPAM film as a function of temperature. Cartoons indicate the correspon-ding state (swollen or collapsed) of the film vs. temperature. Red markers represent the initial heating of the substrate, while blue markers represent data taken during subsequent cooling.

Molecular Self-Assembly in Block Co-Polymers

H-H. Wang, *Argonne National Laboratory*
A. Habenschuss, *Oak Ridge National Laboratory*
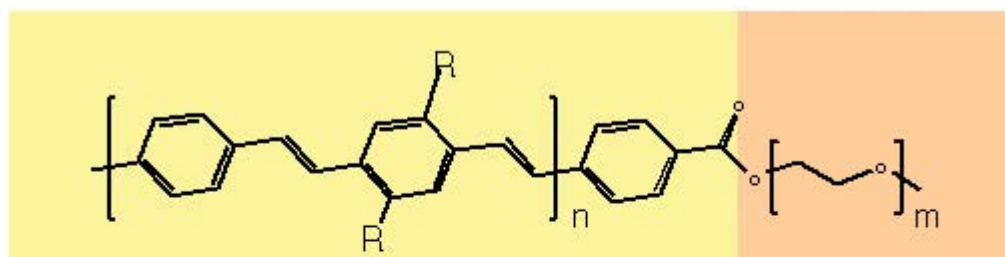***J-H. Chang, Y. Shin,*** *and* ***G.J. Exarhos,*** *Pacific Northwest National Laboratory*

Motivation—Interactions among hydrophilic and hydrophobic chemical blocks that comprise a polymer chain will drive self-assembly into ordered molecular architectures. The resulting high surface area polymer shows phase-separated domain nanostructures formed upon congregation of blocks with similar chemical functionality. Self-assembly in these systems is controlled by the total copolymer length (molecular weight), the magnitude of the pair-wise block interaction parameters (χ_{ij}), and the block lengths that comprise the precursor polymer. Understanding how composition and processing parameters influence the self-assembly process is key to developing phase-separated systems that can function as conducting molecular wires, selective ion traps, efficient catalysts, or enzyme simulants.

Accomplishment—Diblock copolymers have been developed that spontaneously organize into molecular wires in the presence of certain solvents. Under the proper processing conditions, the hydrophilic blocks are found to form a cladding around the more hydrophobic regions. When highly conjugated hydrophobic chemical groups are present in the block, the resulting self-assembled structure resembles a conducting insulated wire where the wire and cladding thickness can be manipulated by changing the composition of the starting polymer. The evolved nanoarchitectures have been characterized by means of transmission electron microscopy and both X-ray and neutron scattering methods. Based upon these measurements, a monolayer (in contrast to bilayer) packing arrangement of the segregated blocks has been determined.

Significance—Work in this project demonstrates how block copolymers can be engineered to self-assemble into targeted architectures. Research probes phase stability regions in these and similar systems that can be associated with the magnitude of local attractions (repulsions) among the constituent blocks in the polymer chain. Results also suggest that certain architectures not usually observed in the diblock system can be achieved upon addition of a single homopolymer. The formalism can be generalized to related systems that contain both hydrophobic and hydrophilic components. For example, self-assembly has recently been observed when low temperature melts of salts and surfactants are allowed to cool. Here, ordering of the constituents is induced by local phase segregation into domains followed by subsequent interaction among the hydrophilic and hydrophobic domains.
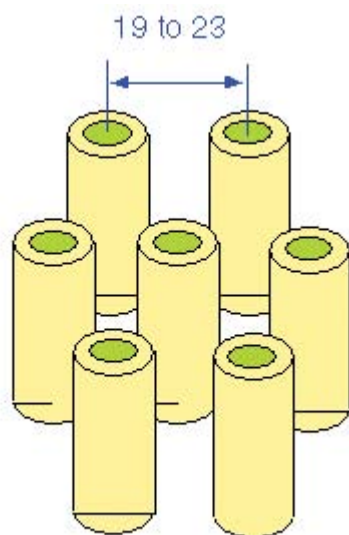
Contact: Hau Wang, Argonne National Laboratory
Phone: (630) 252-3461, Fax: (630) 252-9151, E-mail: hau.wang@anl.gov
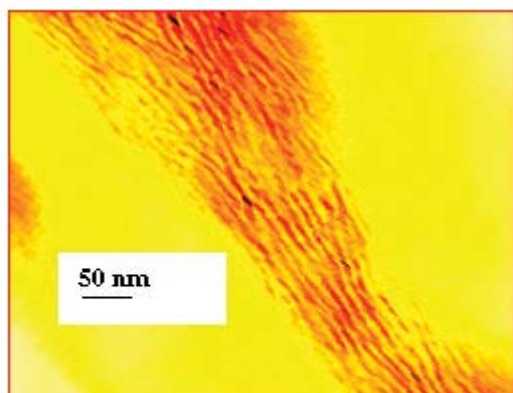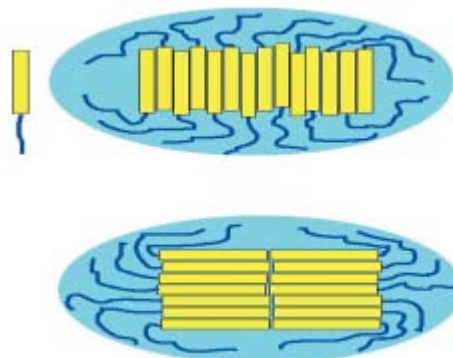
OPV_n - PEG_m R = Hexyl

Hydrophobic Rigid
Photoluminescent
Electroluminescent
Conducting

Hydrophilic Flexible

Packing Motifs

19 to 23

Packed OPV-PEG fibers$_2$ in OTHF/H

50 nm

XRD traces of different polymer compositions

001 11.9 Å   010 4.63 Å

002

003

OPV13PEG45

OPV13PEG13

OPV7   OPV5

Intensity

Intensity

2Theta
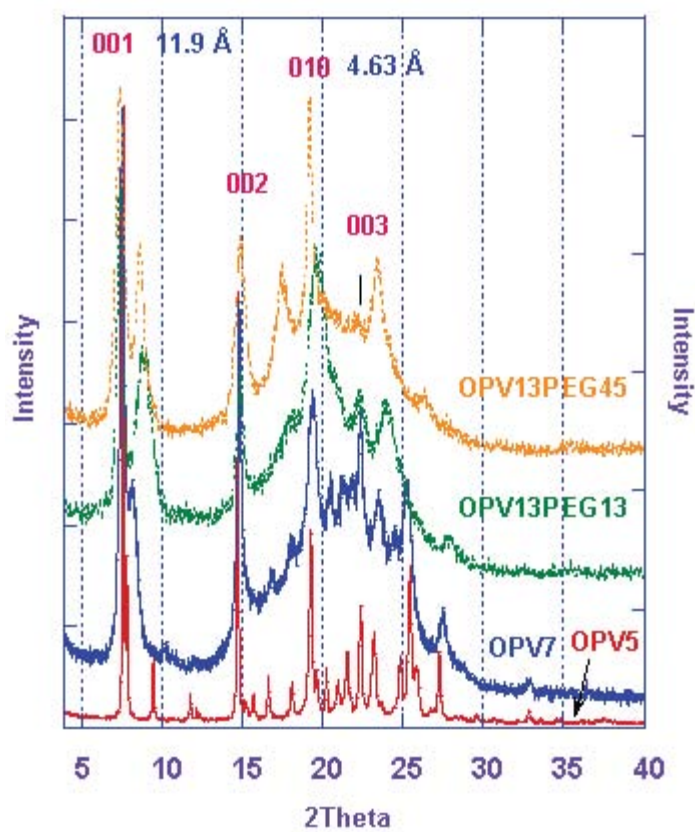
Templateless Assembly of Molecularly Aligned Conducting Polymer Nanowires

Jun Liu, *Sandia National Laboratories, NM*
L. Liang, C.F. Windisch, Jr., Y. Lin, *and* **G.J. Exarhos,** *Pacific Northwest National Laboratory*

Motivation—Many laboratories are actively engaged in the synthesis of electroactive materials based upon oriented carbon nanotubes, or nanowires that are comprised of semiconductors, oxides or metals. An alternate material that can be prepared in high yield involves the electrochemical polymerization of aniline. However, processing approaches to produce high aspect ratio oriented fibers of nanometer dimension have not been successful until only recently. Such materials that exhibit oriented open nanostructures are highly desirable for applications ranging from chemical and biological sensing and diagnosis, energy conversion and storage (photovoltaic cells, batteries and capacitors, and hydrogen storage devices), catalysis, and data storage. The high surface area and high porosity associated with open nanoarchitectures and uniaxial orientation is expected to promote high capacity and enhanced efficiency of these devices.

Accomplishment—Large arrays of uniform and oriented nanowires of conducting polymers on a variety of substrates (Pt, Si, Au, carbon, silica, etc.) have been prepared through controlled nucleation and growth using a step-wise electrochemical deposition process. In this process molecularly-aligned polyaniline molecules assembled into a uniform nanowire array without the use of a templating agent. The step-wise electrochemical deposition method involved an initial stage, in which a high current density was used to induce a large number of nucleation sites on the substrate. The initial stage was followed by a subsequent polymerization step at reduced current density to grow polymer wires from the nucleation sites. The stepwise growth produces uniform oriented nanowires of polyaniline on a variety of flat or rough surfaces. This method for controlled nucleation and growth during electrochemical deposition should also be applicable to other electrochemically active materials.

Significance—The ability to develop oriented nanostructures from electroactive materials has significant technological implications. A chemical sensor (selective for hydrogen peroxide) based on the oriented conducting polymer demonstrated good stability and device reliability under extended operating conditions. The detection of this chemical specie presents a promising approach for glucose biosensor applications.
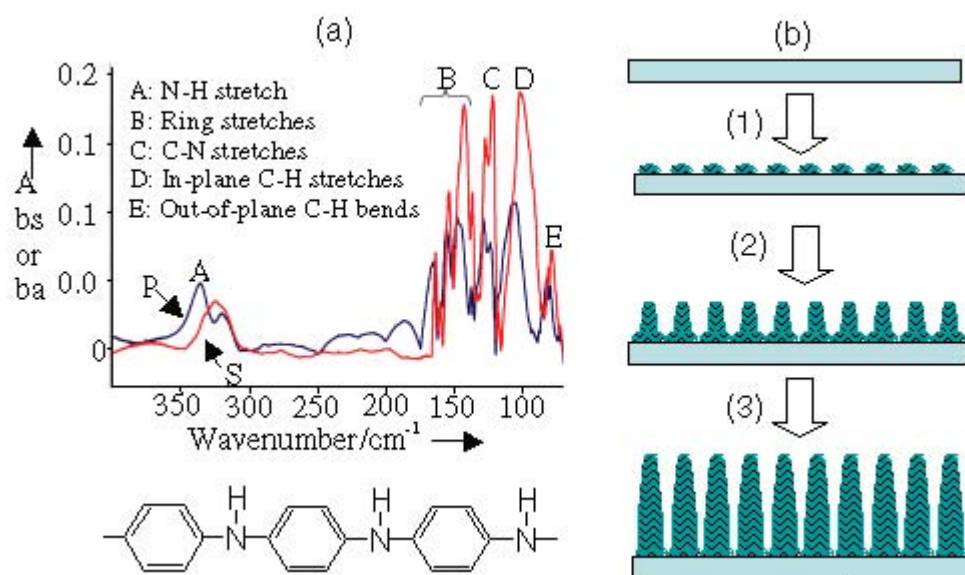
Contact: Jun Liu, Sandia National Laboratories, NM
Phone: (505) 845-9135, Fax: (505) 844-5470, E-mail: jliu@sandia.gov

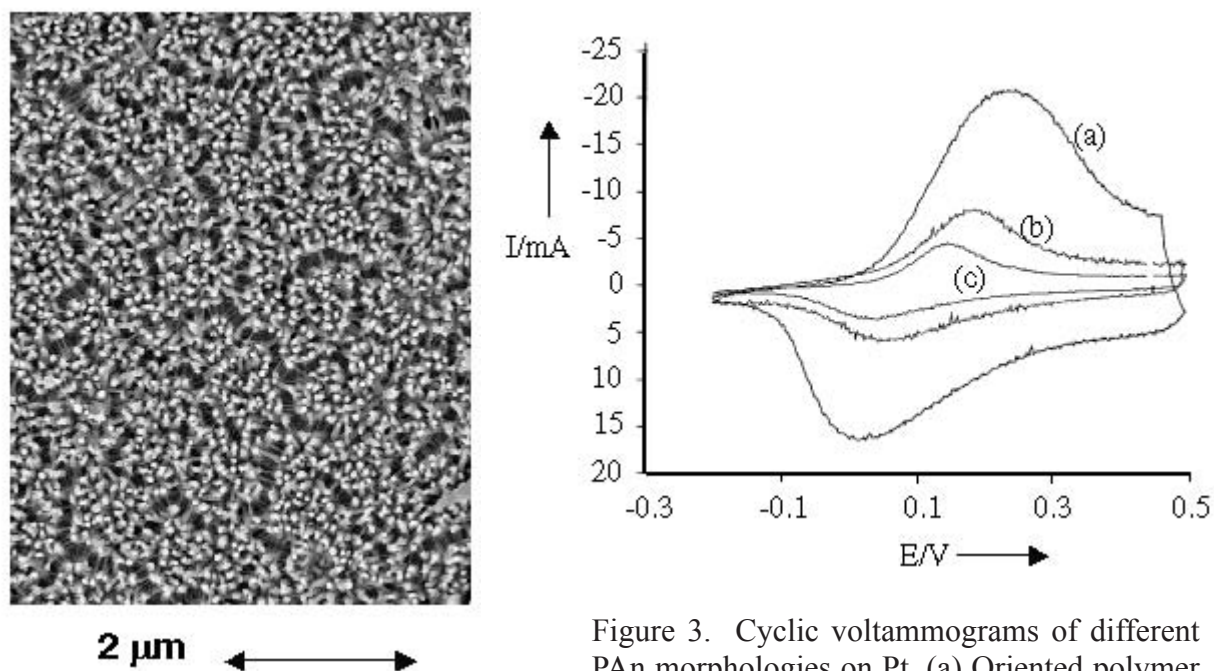Figure 1. IR spectra and polymer growth mechanism.

2 μm

Figure 2. SEM micrograph of oriented polyanile film on Pt.

Figure 3. Cyclic voltammograms of different PAn morphologies on Pt. (a) Oriented polymer nanowires. (b) Randomly-oriented polymer fibers. (c) Dense Polymer films.

High-Toughness Mo-Si-B Refractory Silicide Intermetallic Alloys for Elevated-Temperature Applications

R. O. Ritchie and *H. Choe*, *Lawrence Berkeley National Laboratory*
J. H. Schneibel, *Oak Ridge National Laboratory*

Motivation—The quest for structural materials that can operate at higher and higher temperatures remains a persistent challenge in materials science. One promising system is $MoSi_2$-based silicides, which have good oxidation resistance up to 1700°C and relatively easy processibility; however, like many ordered intermetallics, they are plagued by poor ductility and fracture toughness properties. Boron-containing molybdenum silicides have been the focus of significant research of late due to their potentially superior low-temperature "pest" resistance and high-temperature oxidation resistance due to the formation of borosilicate glass. Of the various multiphase Mo-Si-B intermetallic systems available, alloys with compositions of Mo 12-17Si 8.5B (at.%), which contain Mo, Mo_3Si, and Mo_5SiB_2 (T2) phases (Fig. 1), are anticipated to have higher toughnesses due to the presence of the relatively ductile α-Mo phase. In this study, we examine the ambient to high (1300°C) temperature fracture toughness and fatigue-crack growth characteristics of a series of Mo 12-17Si 8.5B alloys, with the objective of discerning the salient mechanisms governing crack growth.

Accomplishment—The fracture toughness (Fig. 2) and fatigue-crack growth resistance (Fig. 3) of the Mo-Si-B alloys are substantially higher than monolithic $MoSi_2$ both at ambient and elevated temperatures. Moreover, the ingot-metallurgy (I/M) Mo-Si-B alloys with the coarsest particles, highest volume fraction, and most near-continuous distribution of the α-Mo phase, showed by far the best properties. In particular, the I/M Mo-12Si-8.5B alloy (IM1) displays a relatively high intrinsic toughness at 800° up to 1200°C (~10 MPa√m) due to crack trapping toughening mechanism by α-Mo phase, with only limited extrinsic R-curve toughness. Although the lack of extrinsic toughening is not necessarily beneficial, it does imply that a brittle material should show a reduced susceptibility to fatigue failure, as is observed at temperatures up to 1300°C. *Of particular significance is that both the fracture toughness and the fatigue threshold are increased with increasing temperature.* This remarkable property is associated with the onset of additional toughening mechanisms that become active at high temperatures, specifically involving crack bridging by the α-Mo phase and microcracking primarily in the Mo_5SiB_2 phase (Fig. 2).

Significance—Mo-Si-B silicide alloys can be processed with considerably higher, tougheness (>12 MPa√m) and more fatigue resistance (fatigue threshold ~7 more MPa√m) than monolithic $MoSi_2$ and its alloys. Moreover, their crack-growth resistance, in both fracture and fatigue, progressively increases with increases in temperature up to 1300°C. The improved mechanical properties of these alloys coupled with their improved pest resistance indicate exceptional promise as engine materials for propulsion systems that operate with metal temperatures well above 1000°C.

Contact: R. O. Ritchie, Lawrence Berkeley National Laboratory
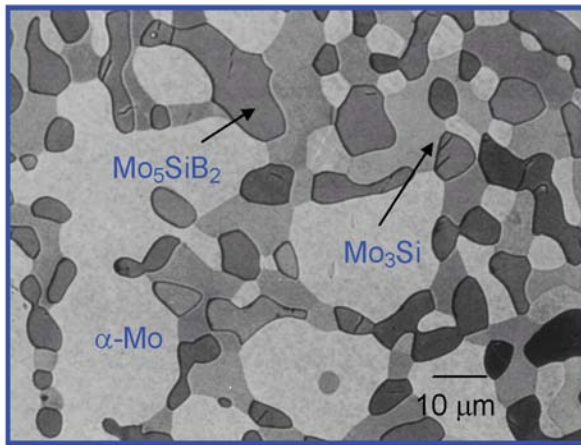Phone: (510) 486-5798, Fax: (510)-486-4881, E-mail: roritchie@lbl.gov

Figure 1. Scanning electron micrograph of the Mo-12Si-8.5B (at.%) alloy (IM1), showing α-Mo particles in an intermetallic matrix of Mo_3Si and Mo_5SiB_2 (T2).
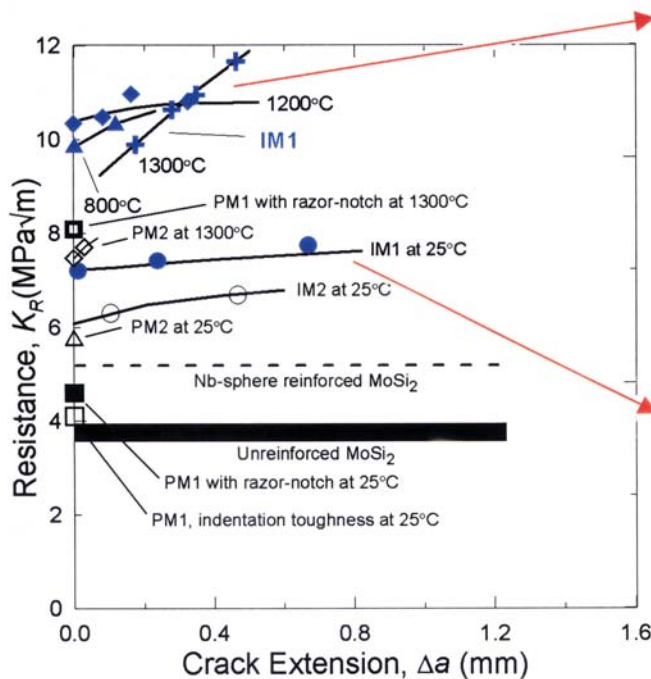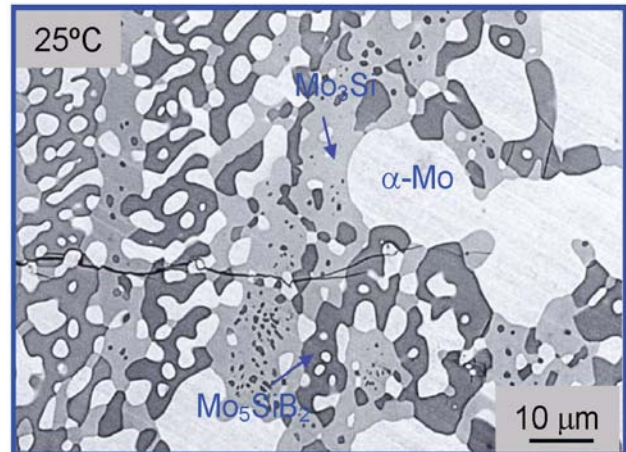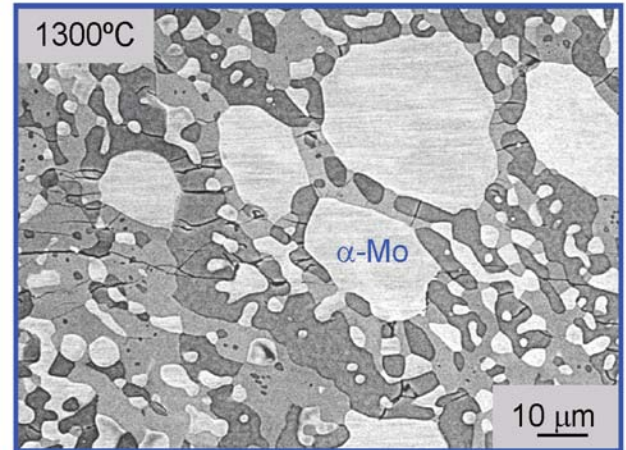

Figure 2. Fracture toughness behavior, in the form of K_R (Δa) crack-growth resistance curves, for Mo-Si-B alloys both at ambient and elevated temperatures, as compared to monolithic $MoSi_2$ and $MoSi_2$ reinforced with Nb spheres.

Figure 3. Cyclic fatigue-crack propagation data for a series of Mo-Si-B alloys as a function of the applied K_{max} and ΔK at 25°C, 800°C, 1200°C, and 1300°C, compared to monolithic $MoSi_2$ and $MoSi_2$ reinforced with Nb spheres.
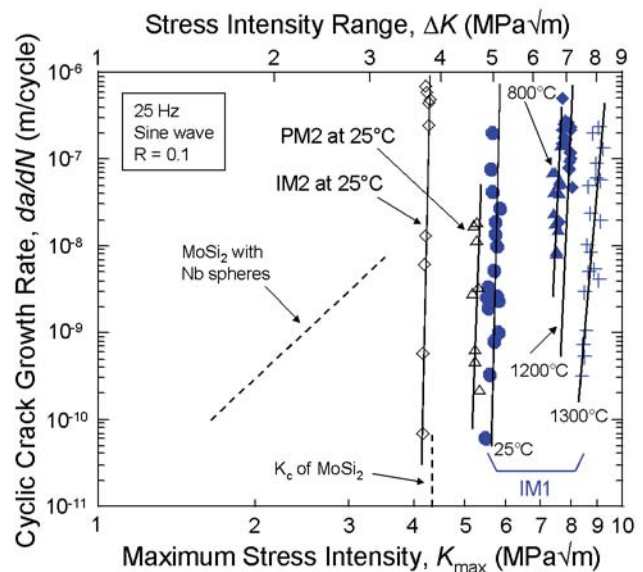
Processing, Microstructure, and Creep Strength of Molydenum-Silicon-Boron Intermetallics

J. H. Schneibel, Oak Ridge National Laboratory
M. J. Kramer, Ames Laboratory

Motivation—The creep strength of multi-phase alloys is determined not only by the volume fraction, but also by the size and spatial distribution of the different phases. Because of recent progress in processing, Mo-Si-B alloys with a wide range of microstructures and microstructural scales can be produced. The present work was motivated by the need to understand the variations in the creep strength as a function of microstructure.

Accomplishment—Three different alloys consisting of α-Mo (Mo solid solution), Mo_3Si, and Mo_5SiB_2 were processed. Arc-cast ingots were ground into powder which was consolidated by hot isostatic pressing. Alloy 1 contained 21 vol.% of isolated α-Mo particles. Alloy 2 had the same nominal composition as alloy 1, but was prepared from a mixture of Mo_3Si/Mo_5SiB_2 and Mo powder. Alloy 3 was prepared from Mo_3Si/Mo_5SiB_2 powder which was "coated" with α-Mo by removing Si by vacuum annealing, as described in last year's brief. The α-Mo volume fraction of this alloy was 30%. Figure 1 shows SEM micrographs of the microstructures of all three alloys. It illustrates the fine isolated α-Mo particles in alloy 1, the coarse, elongated α-Mo particles in alloy 2, and the fully continuous α-Mo matrix of alloy 3. Figure 2 compares the creep strength of the three alloys as measured by the compressive flow stress at a strain rate of 10^{-5} s^{-1} and a plastic strain of 2%. The different alloys show very different behavior which can be qualitatively understood in terms of their microstructural topology and scale. Alloy 1 has a very fine microstructure corresponding to a high density of high-diffusivity grain boundaries and interfaces. As a result, it is weak at high temperatures (1400°C). Also, it exhibits a stress exponent near 2 that is typical of fine-grained superplastic materials. At lower temperatures (1200°C) its strength is slightly lower that that of alloy 2 which has also a continuous Mo_3Si/Mo_5SiB_2 matrix, but a larger microstructural scale. At 1200°C alloy 3 is much weaker than alloy 2 because its strength is determined by the continuous α-Mo matrix which is relatively weak at 1200°C. At higher temperatures the strengths of Mo_3Si and Mo_5Si_3 decrease significantly and therefore the strengths of alloys 2 and 3 become comparable.

Significance—This work shows that the high temperature strength of Mo-Si-B alloys depends strongly on the topology and scale of their microstructure. For comparable compositions, the creep strength can be varied by a factor of two by manipulating the microstructure and its scale. Microstructural topology and scale also influence other properties such as fracture toughness and oxidation resistance, but not necessarily in the same way as the creep strength. For example, alloy 1 exhibits very good oxidation resistance because the α-Mo particles are small and isolated, but its creep strength at 1400°C is poor. Balancing the requirements for properties such as fracture toughness, oxidation, and creep strength requires a detailed understanding of the influence of the microstructure. The present work provides an example of this interrelationship between processing, microstructure, and properties.

Contact: J. H. Schneibel, Oak Ridge National Laboratory
Phone: (865) 576-4644; Fax: (865)-574-7659; E-mail: schneibeljh@ornl.gov

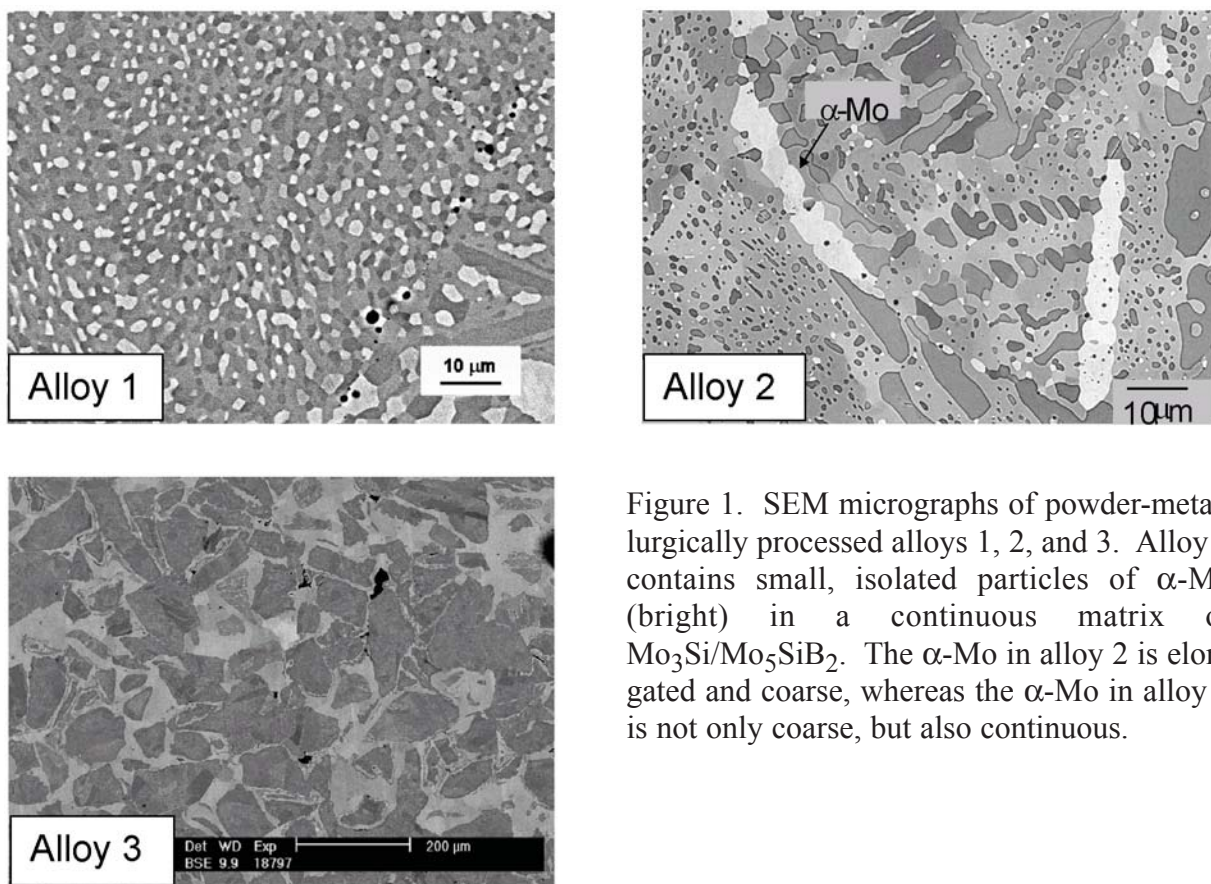Figure 1. SEM micrographs of powder-metallurgically processed alloys 1, 2, and 3. Alloy 1 contains small, isolated particles of α-Mo (bright) in a continuous matrix of Mo_3Si/Mo_5SiB_2. The α-Mo in alloy 2 is elongated and coarse, whereas the α-Mo in alloy 3 is not only coarse, but also continuous.
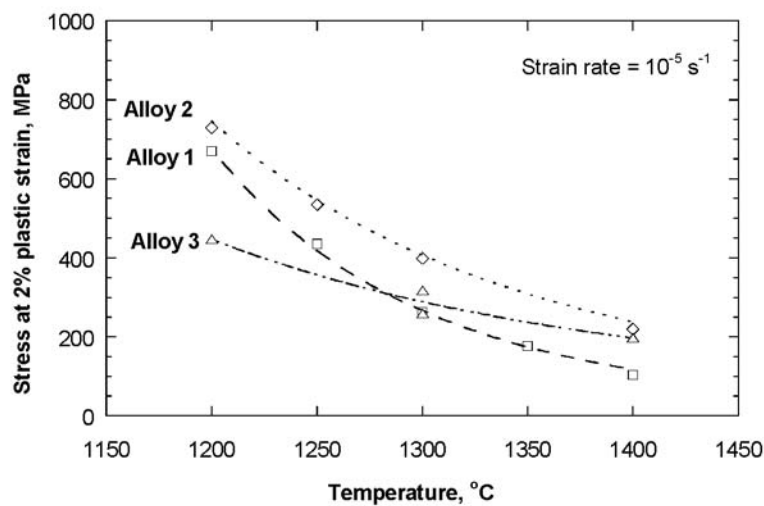

Figure 2. High-temperature creep strengths of the alloys with the microstructures in Fig. 1.

Oxidation and Corrosion Behavior of High Temperature Mo-Si-B Alloys

A. J. Thom, M. J. Kramer, and *M. Akinc, Ames Laboratory*
J. H. Schneibel and *P. F. Tortorelli, Oak Ridge National Laboratory*
K. Natesan, Argonne National Laboratory

Motivation—Multiphase composite alloys based on the Mo-Si-B system are candidate materials for high temperature applications. The $Mo_5Si_3B_x$ (T1) phase imparts excellent oxidation resistance and creep strength but suffers from brittle fracture. Incorporating the bcc-Mo phase significantly improves fracture toughness, but reduces oxidation resistance. Successful components based on these multiphase assemblages must function in aggressive combustion environments, so this study seeks to better understand their oxidation and corrosion behavior.

Accomplishment—Three phase assemblages were studied: $T1\text{-}MoB\text{-}MoSi_2$, $T1\text{-}Mo_5SiB_2$ (T2)-Mo_3Si, and $Mo\text{-}T2\text{-}Mo_3Si$. Fig. 1 shows that during isothermal oxidation in dry air at 1100°C, all alloys underwent an initial mass loss due to formation and volatilization of MoO_3. The magnitude of these initial losses varied according to the alloy's overall Mo content, and all alloys assumed a near-zero, steady-state mass change following the initial loss. The corresponding micrographs show that all alloys formed a continuous, borosilicate scale. Fig. 2 shows the oxidation of material at 1200°C in dry air using cycles of 60 min at temperature and 10 min out of the furnace. Also tested was $MoSi_2$

for comparison. After an initial mass loss, the $T1\text{-}MoB\text{-}MoSi_2$ alloy showed a slow mass gain comparable to $MoSi_2$. The $T1\text{-}T2\text{-}Mo_3Si$ alloy showed a continual mass loss, while the $Mo\text{-}T2\text{-}Mo_3Si$ alloy had a larger initial mass loss, followed by a much slower mass loss. All alloys were covered with a glassy scale, but only the $T1\text{-}MoB\text{-}MoSi_2$ alloy formed a continuous sub-scale silica layer. Fig. 3 shows the sulfidation of the $T1\text{-}MoB\text{-}MoSi_2$ alloy in a 1.5 vol% $H_2S\text{-}H_2$ gas mixture. Mo sulfide formed on the surface at 500°C, and by 1100°C it almost completely covered the alloy.

Significance—During isothermal oxidation, a protective scale forms that significantly reduces oxygen transport to allow formation of Mo and MoO_2 precipitates at the scale/alloy interface. Higher Si content multiphase assemblages more readily form a protective silica-containing scale during cyclic oxidation. Preliminary sulfidation tests indicate that alloys can develop protective sulfide scales during service in reducing environments. These results suggest that a component design strategy of coating a $Mo\text{-}T2\text{-}Mo_3Si$ substrate with a $T1\text{-}MoB\text{-}MoSi_2$ coating may provide a desirable balance of fracture toughness and resistance to oxidation and corrosion.

Contact: A. J. Thom, Ames Laboratory
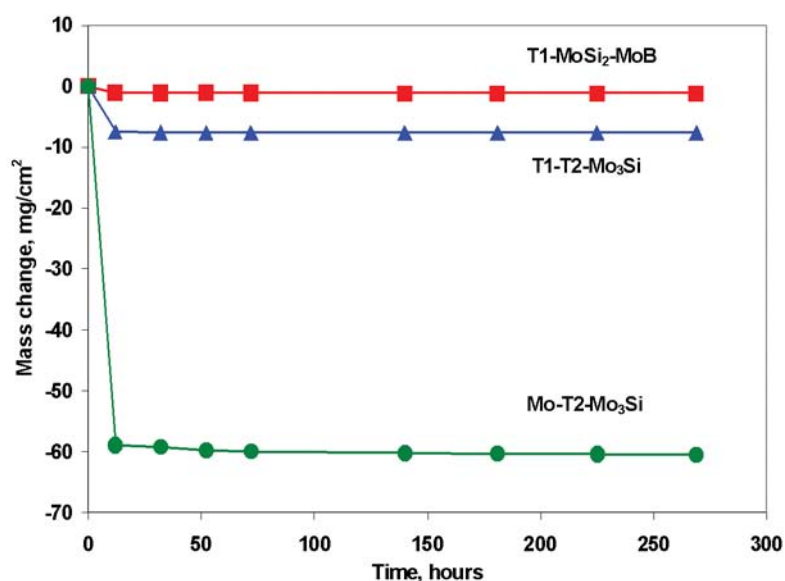Phone: (515) 294-4064, Fax: (515) 294-4709, E-mail: ajthom@ameslab.gov

Figure 1. Mass change in dry air during isothermal oxidation for Mo-Si-B alloys at 1100°C. Micrographs show cross-section of the scale formed on each alloy.
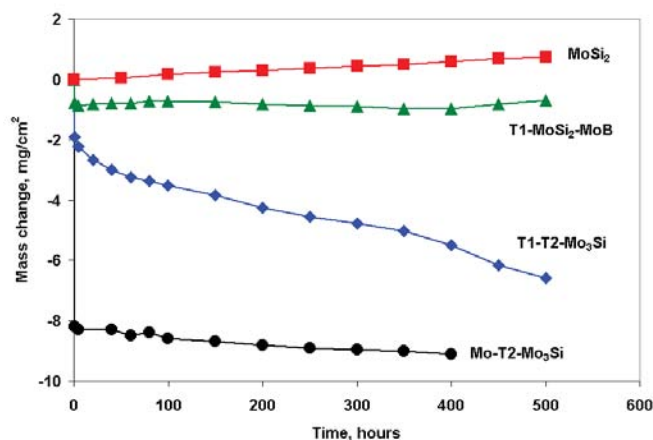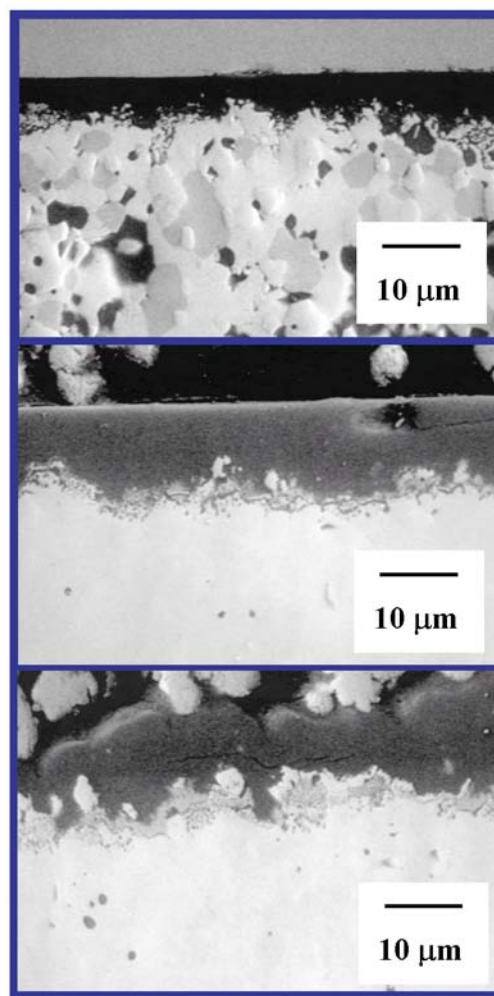

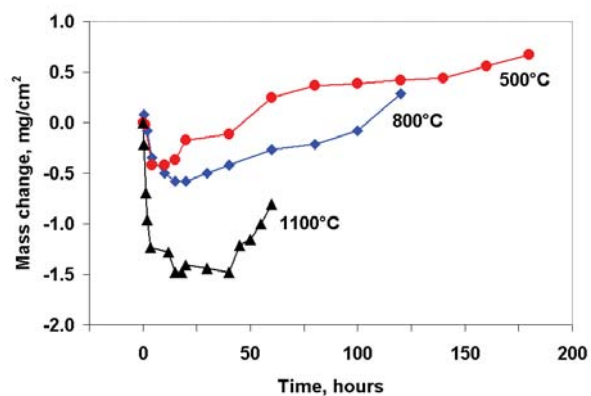Figure 2. Mass change in dry air during cyclic oxidation for Mo-Si-B alloys at 1200°C.

Figure 3. Mass change for Mo-Si-B alloy during sulfidation in 1.5 vol. % H_2S-H_2 gas mixture.

In-Situ Synchrotron X-Ray Studies of Metal-Organic Chemical Vapor Deposited PbTiO$_3$ Thin Films

G. B. Stephenson, S. K. Streiffer, O. Auciello, M. V. Ramana Murty, D. D. Fong,
J. A. Eastman, and A. Munkholm, Argonne National Laboratory
Carol Thompson, Northern Illinois University

Motivation—Lead-based perovskites such as Pb(Zr$_x$Ti$_{1-x}$)O$_3$ are leading candidates for applications in ferroelectric nonvolatile memories as well as pyroelectric and piezoelectric devices. For high-density integration onto nonplanar structures, metal- organic chemical-vapor deposition (MOCVD) is the preferred synthesis route for these materials. Better understanding of the growth mechanisms involved could lead to improvements that facilitate integration into semiconductor manufacturing. In addition, the progressive miniaturization of these structures leads to concerns about the effect of surfaces on the ferroelectric phase transitions. However, little is known about the atomic-scale mechanisms of MOCVD of multicomponent oxides or their surface structures.

Accomplishment—We have constructed a unique apparatus to carry out *in situ*, real-time x-ray scattering investigations of MOCVD of Pb-based perovskites (Figure 1(a)) [1]. Here we focus on the prototypical perovskite, PbTiO$_3$, which is grown using the precursors tetraethyl lead (TEL) and titanium isopropoxide (TIP). A careful analysis of features in the scattering pattern known as "crystal truncation rods" (CTRs) allows us to determine both the growth mode during MOCVD and the PbTiO$_3$ surface structure.

Figure 1(b) shows the evolution of the 20*L* CTR intensity at $L = 0.5$ during deposition at 735 ºC, at various TIP and TEL flows [2]. The data indicate that layer-by-layer growth occurs at the faster growth rates; as the growth rate is reduced, the mode changes to step-flow. This is the first demonstration of step-flow growth for MOCVD of a perovskite. Further experiments have shown that within the range of tempera-

tures studied (650 and 735 ºC), the rate of growth is limited only by Ti transport and is independent of temperature, TEL flow, and P_{O2}. We find that films with the smoothest surface morphology result from growth with high TIP/TEL ratios, with P_{TEL} not much larger than the equilibrium vapor pressure of PbO over PbTiO$_3$.

We have also determined the equilibrium surface phase diagram of PbTiO$_3$ (001) as a function of temperature and PbO vapor pressure (Figure 2(a)) [3]. Across the complete bulk PbTiO$_3$ single-phase field, the surface structure was found to have $c(2\times2)$ symmetry. The equilibrium $c(2\times2)$ phase consists of a single-unit-cell layer with an antiferrodistortive structure obtained by oxygen octahedra rotations in the TiO$_2$ plane (Figure 2(b)).

Significance—Further advances in the miniaturization of ferroelectric devices require a better understanding of the growth and phase transition behavior of ferroelectric films. By *in-situ* x-ray scattering, we have determined the optimum conditions for MOCVD of PbTiO$_3$ and demonstrated that it is possible to achieve layer-by-layer and step-flow growth during MOCVD of a multicomponent oxide. The discovery of the antiferrodistortive surface structure may help us understand the often observed decrease in ferroelectric character in thin films.

1. G. B. Stephenson et al. *MRS Bull.* **24**(1), 21 (1999).
2. M. V. Ramana Murty et al. *Appl. Phys. Lett.* **80,** 1809 (2002).
3. A. Munkholm et al. *Phys. Rev. Lett.* **88,** 016101 (2002).4. I. Barin, *Thermochemical Data of Pure Substances* (VCH, New York, 1995), 3rd ed.

Contact: G. B. Stephenson, Argonne National Laboratory
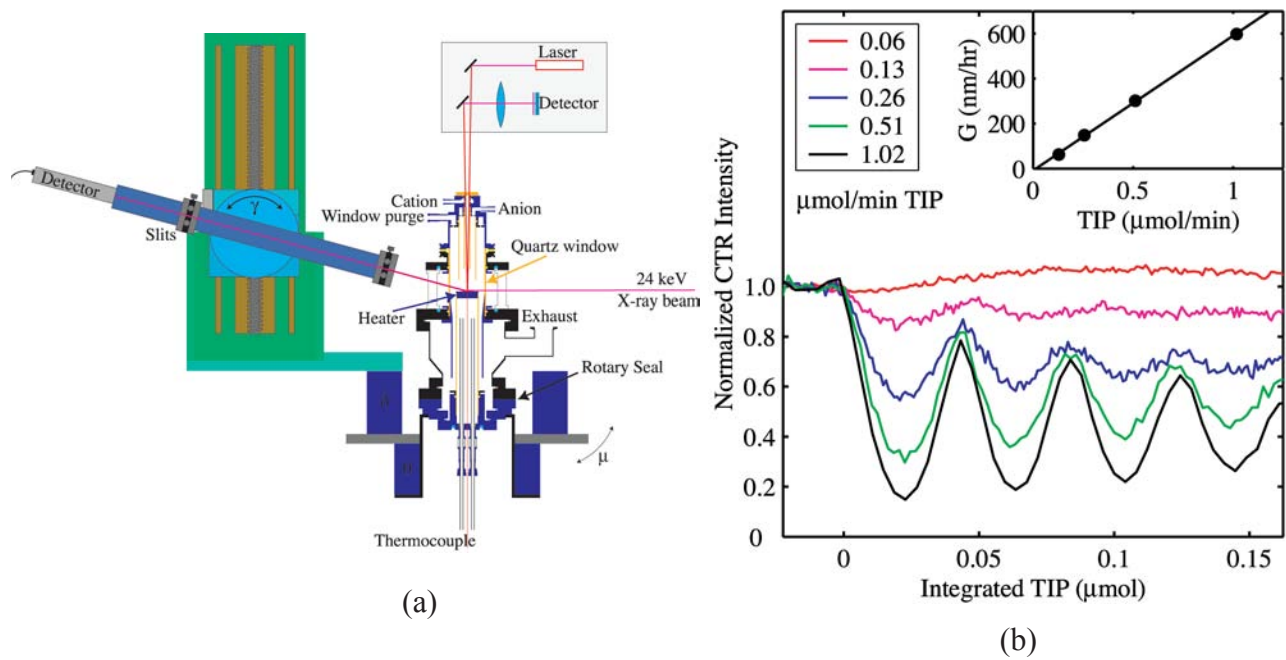Phone: (630) 252-3214, Fax: (630) 252-7777, E-mail: stephenson@anl.gov

(a)

(b)

Figure 1. (a) Schematic of the MOCVD chamber established at beamline 12-ID-D at the Advanced Photon Source. (b) Evolution of the 2 0 0.5 CTR intensity during PbTiO$_3$ growth at various TIP flow rates, for a fixed TIP/TEL ratio of 1.0 during growth and $T = 735$ °C. Curves are plotted vs. integrated TIP flow to show all on the same scale. Inset: growth rate, G, is proportional to precursor supply.

(a)

(b)
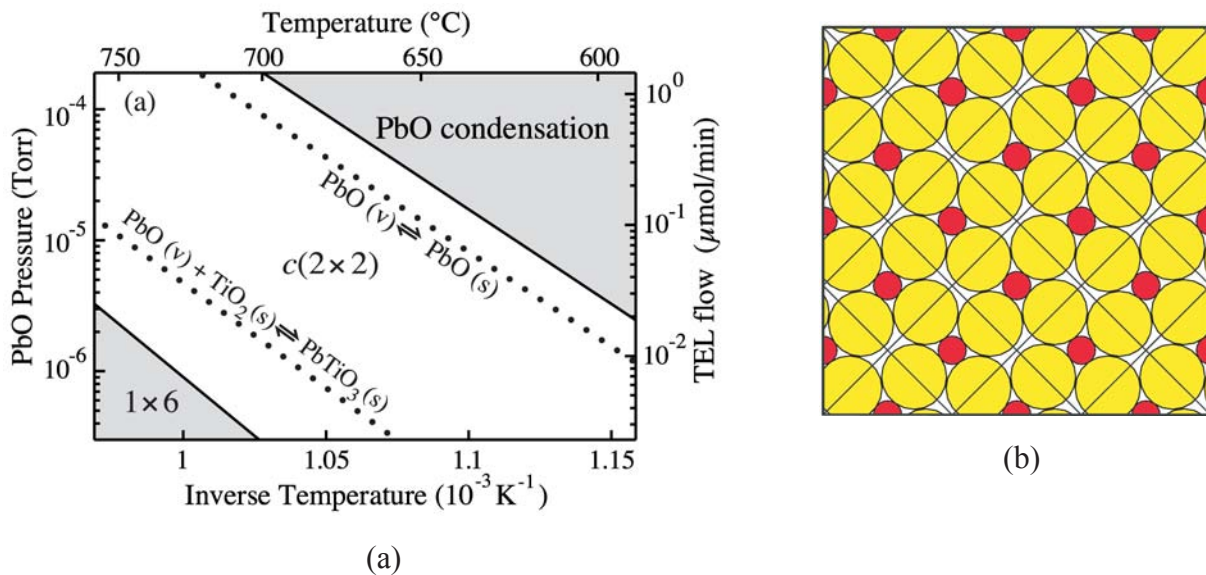
Figure 2. (a) Equilibrium phase diagram of the PbTiO$_3$ (001) surface showing the region investigated. Solid lines separate phase fields corresponding to PbO condensation, $c(2\times2)$ and 1×6 reconstructions. Dotted lines are literature values [4] for the PbO condensation and PbTiO3 decomposition boundaries. (b) Schematic of the TiO$_2$ layer (Ti in red, O in yellow) in the $c(2\times2)$ PbTiO$_3$ (001) reconstruction, showing counter-rotated O cages. The square grid shows the underlying bulk PbTiO$_3$ unit cells.

In Situ Real-Time Studies of Complex Oxide Thin Films

A.H. Mueller, N.A. Suvorova and *E.A. Irene,* Univ. of North Carolina
O. Auciello, Argonne National Laboratory

Motivation—Perovskite and other complex oxide thin films usually form intermixed interfacial layers when deposited upon most substrates. Typically the interfacial layers are not only chemically different from the substrate and the oxide overlayer, but they also have different electronic properties. For high static dielectric constant (ε) films, the interface layers usually have a lower ε than the film and thus reduce the effective ε for the stack. Also, ferroelectric and piezoelectric properties are similarly degraded in the interface region.

Thus, developing an understanding of the formation dynamics of interfacial layers and an ability to control the layers is crucial to technologies based on complex oxides. However, because the interface is covered by an overlayer during film deposition, it is difficult to unambiguously characterize. To this end, our research has focused on *in-situ*, real-time characterization of interface formation during complex oxide film deposition.

Accomplishment—Initially, we designed and implemented a unique film deposition and complementary *in situ* real-time characterization system, as illustrated in Fig. 1. Multiple target reactive ion sputtering is used for film deposition, and spectroscopic ellipsometry (SE) is combined with time of flight ion scattering and recoil spectrometry (ToF-ISARS) for complementary real-time characterization while depositing. A large variety of complex materials can be prepared, and the as-deposited layers can be mass and structure analyzed using ToF-ISARS while the growth dynamics and optical properties are obtained using SE.

During deposition of barium strontium titanate (BST) on both Si and SiO_2 surfaces, an intermixed interface layer was observed to form. Figure 2 (left panel) compares the growth dynamics for BST on the Si and SiO_2 surfaces showing both the evolution of the intermixed interface layer and the BST layer. For bare Si, the interface layer forms first to about 22 Å and then BST forms. For the SiO_2 surface, the interface layer commences to grow subcutaneously after about 5 min BST deposition. Figure 2 (right panel) shows the composition evolution during growth. Si is seen at the surface after substantial BST deposition for both substrates. This indicates that BST reacts with both Si and SiO_2 albeit more so with Si.

We have discovered that there is a hyperbolic relationship between ε for the BST overlayer and ε for the interface layer. This relationship can lead to large errors in determining dielectric constant of the film from capacitance-voltage measurements. Electronic measurements of BST grown on both substrates demonstrate that interface charge and surface electronic states are better with SiO_2 substrates.

Significance—The ability to perform *in-situ*, real-time characterization of interface formation during complex oxide film deposition enables accurate information about critical interface evolution to be gained. This information has enabled the formulation of a model for interface formation and has provided guidance for the ongoing optimization studies of high ε dielectrics.

Contact: Eugene A. Irene, University of North Carolina
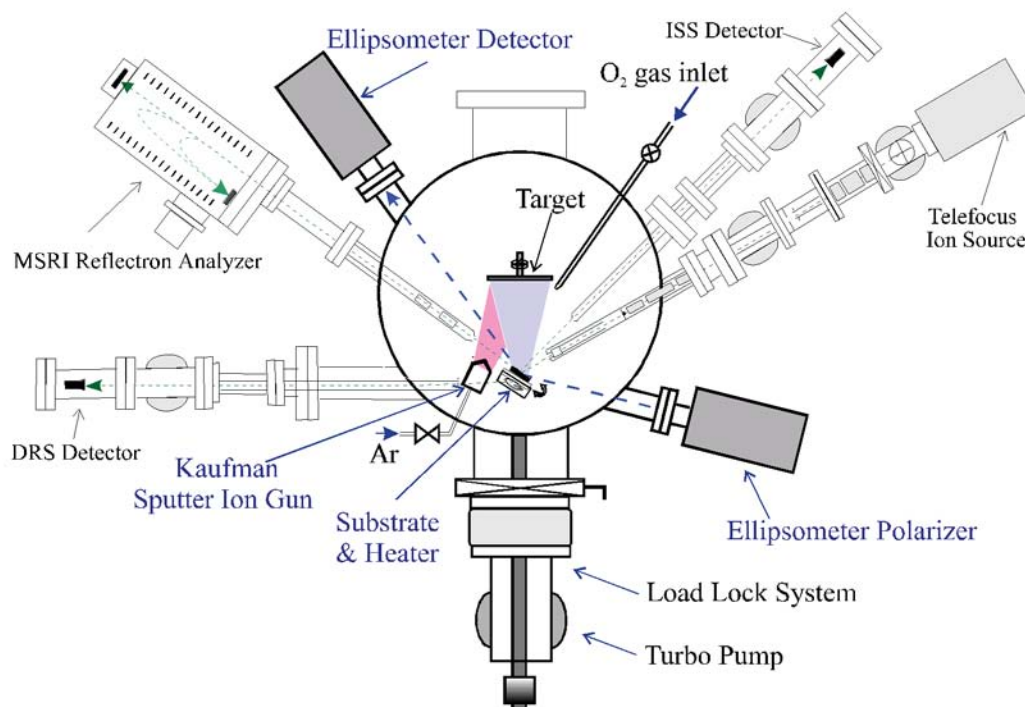Phone: (919) 966-1652, Fax: (919) 962-2388, E-mail: gene_irene@unc.edu

Figure 1. Schematic of ion beam deposition system with spectroscopic ellipsometry (SE) and time of flight ion scattering and recoil spectrometry (ToF - ISARS)
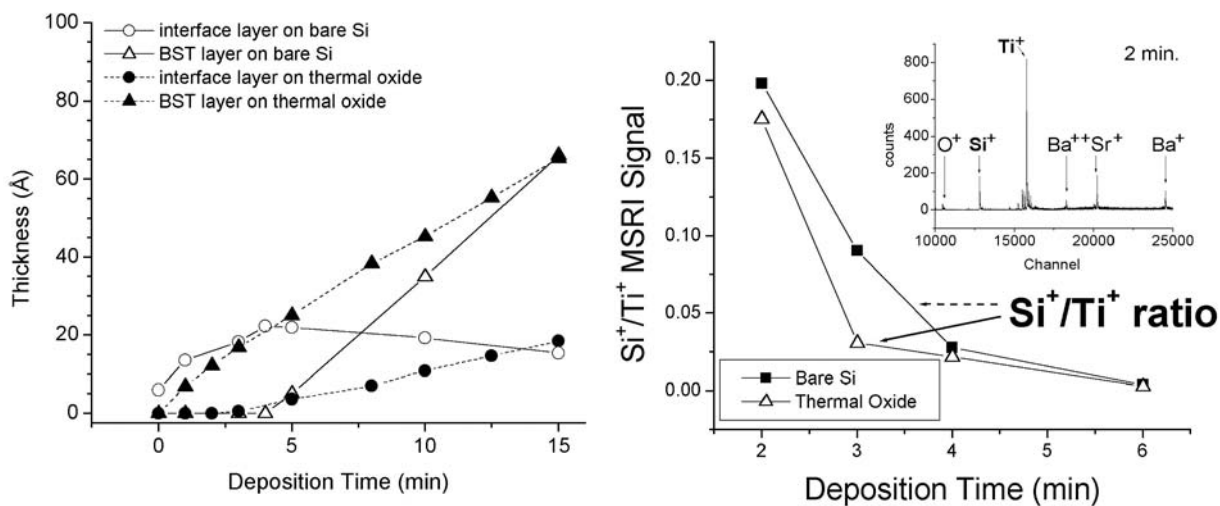

Figure 2. Left Panel: SE results for BST deposition at 450oC on bare Si and SiO2 substrates; Right Panel: Mass spectrum of recoiled ions data for the depositions in terms of the Si+/Ti+ ratio.

Piezoelectric Behavior of Nanoscale Epitaxial PZT Thin Film Capacitors

V. Nagarajan, A. Stanishevsky, T. Zhao, S. Prasertchoung, L. Chen, J. Melngailis,
A. Roytburd and *R. Ramesh,* *University of Maryland*
Orlando Auciello, *Argonne National Laboratory*

$\mathbf{M}$otivation—The $PbZr_xTi_{1-x}O_3$ (PZT) family of compounds have been used in bulk piezoelectric applications for several decades. However, during the past decade the focus and demand has switched from bulk to thin film sensors and actuators that can be integrated with the mature Si based IC technology. Unfortunately, in thin films, the piezoelectric response has been observed to be much lower than in bulk. This effect has been generally attributed to substrate-induced constraints. The decrease in surface displacement due to clamping by substrate has been calculated, and is directly related to the compliances of the PZT film and the substrate. The motivation for the present work is two-fold. Primarily we investigated the possibility of achieving theoretically predicted single-crystal, single-domain *(intrinisc)* values for d_{33} by the eliminating the substrate induced constraint. Secondly, we investigated the piezoelectric behavior of capacitors in the sub-micron regime, a hitherto unknown behavior that needs understanding.

$\mathbf{A}$ccomplishment—In order to be able to compare experimentally determined piezo-coefficients to theoretical predictions, it is imperative to be able to create model systems consisting of single crystalline films of carefully controlled compositions. Furthermore, it is equally important to understand such behavior in films deposited on technologically relevant substrates such as Si. We have been able to accomplish this through the use of a novel template approach to oxide heteroepitaxy on Si. Furthermore, nanoscale capacitors were fabricated via Focused Ion Beam (FIB) milling as shown in Fig. 1. By this technique we have achieved capacitors as small as 70nm in diameter. Figure 2 shows the piezoelectric d_{33} loop measured for a 0.5 micron capacitor and a 50 micron capacitor of $PbZr_{0.5}Ti_{0.5}O_3$ composition. On the same plot we also show the d_{33} field dependence predicted by theory for a fully unclamped case and a fully clamped case. Clearly for the 0.5 micron capacitor at remanence, we have achieved the predicted intrinsic value. However, there is a more rapid drop in d_{33} with field for the experiment compared to that predicted by theory at large fields. In contrast, the fully clamped 50μm capacitor behaves exactly as the model predicts. The anomalous behavior of the 0.5μm film needs to be further understood.

$\mathbf{S}$ignificance—With the push towards high-density memories and nanoscale electromechanical systems (NEMS) it is imperative to understand piezoelectric behavior at very small scales. We have now developed a fabrication technique to enable these studies. This work has led to the observation of a novel field dependent behavior, especially in PZT compositions close to the Morphotrophic Phase Boundary.

Contact: Nagarajan Valanoor, University of Maryland
Phone: (301) 405-6552, Fax: (301) 314-7136, E-mail: etop@glue.umd.edu
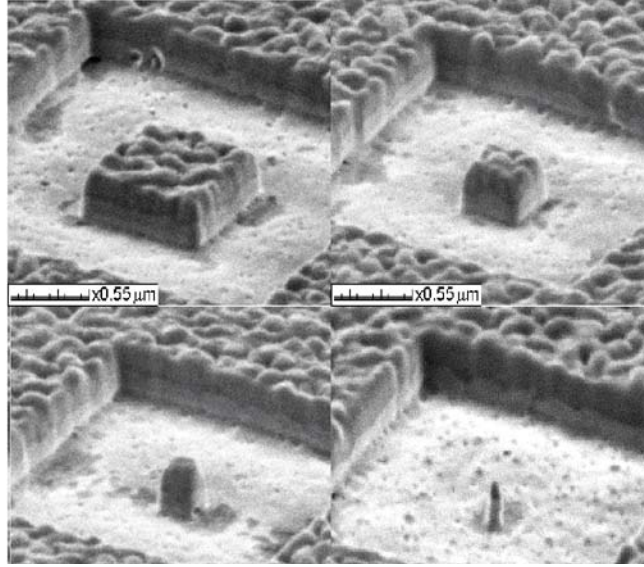
Figure 1. SEM images of nanoscale devices fabricated via Focused Ion Beam (FIB) milling.

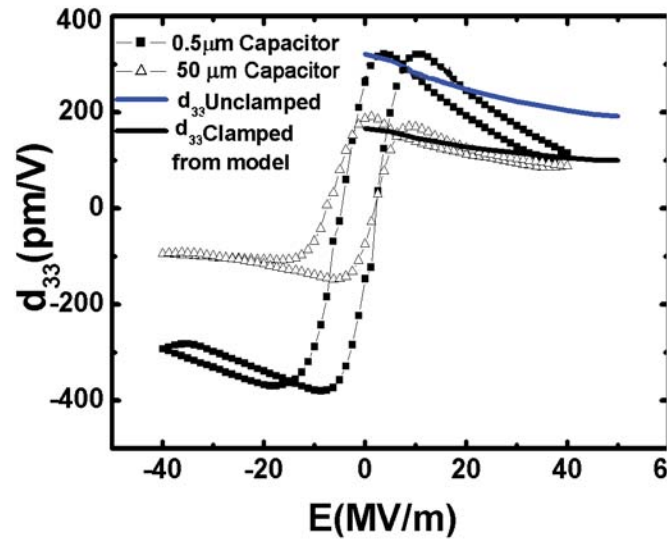

Figure 2. Piezoelectric behavior: 0.5 micron FIB milled capacitor, a 50 micron capacitor and theoretical d_{33} vs. field.

Interface Materials Physics for Oxide/Semiconductor Nanosystems

R. McKee, F. Walker, M. Chisholm, B. Shelton, and *M. Stocks, Oak Ridge National Laboratory*
Marco Buongiorno Nardelli, North Carolina State University
Duane Goodner, and *Mike Bedzyk, Northwestern University*
Orlando Auciello, Argonne National Laboratory

Motivation—The goal of our research in thin-film oxides is to study the physics associated with length scale phenomena in ferroelectricity, in particular the fundamental length scales that control phase stability. We have been advancing this goal through this Center collaboration between universities and National Laboratories.

Accomplishment—These collaborative efforts are all involved in utilization of crystalline oxides on semiconductors (COS) to study cooperative phenomena in oxides and their coupling to the charge state of an underlying semiconductor - interface electrostatics at the atomic level. Figure 1 illustrates data that relates to the fundamentals of physical/electrical structure coupling at COS interfaces. In this report, we present recent results on interface formation and its influence on electrostatics at alkaline earth oxide/semiconductor interfaces.

While it was recognized in our early experiments that the oxide/semiconductor epitaxy was controlled by as little as 1/4 of an atomic layer at the interface, first principles theory (ORNL and NCSU) has now revealed an unexpected "Coulomb Buffer" between the materials. X-ray standing wave experiments done at Northwestern Univ. and Argonne using the APS are demonstrating that the effect of the Coulomb Buffer is to place and displace the interface atoms, uniquely "fixing" the electrostatic boundary conditions for a stable semiconductor/oxide structure. Both theoretical and experimental work are proceeding to further clarify this new effect and its potential as input for designing nanoscale materials systems, but this experi-

ment/theory synergism has already provided the first demonstration of how structure-specific chemical bonding in a sub-monolayer phase can be fundamental to balancing the relative electrostatic potential at dielectric/semiconductor interfaces.

Figure 2 shows Z-contrast, chemical and structural arrangement associated with chemical bonding and epitaxy at the interface between the alkaline earth oxide and silicon. Our 1st principles calculations describe the adjustment of the electrostatic potential across the interface that in-turn is responsible for the valence band offset and alignment data in Fig. 1. The coulombic interaction between the materials "buffers" the electrical coupling in a unique and predictable way. The silicide layer is the interface phase. Its structure and bonding to the silicon and the oxide is not expected from the bulk terminations of the two adjoining lattices.

Significance—We believe that this is the first treatment of the band-offset problem that is based on quantitative experimental information about interfacial structure. With this structure information, we have combined surface and interface thermodynamics along with in-situ XPS characterization of band-edge alignment and first principle self-consistent energy calculations based on standard Density Functional Theory (DFT) in the Local Density Approximation (LDA) to show that an interface phase (not simply a bulk termination junction) defines the electrostatic boundary conditions based on commensurate heteroepitaxy.

Contact: Rodney McKee, Oak Ridge National Laboratory
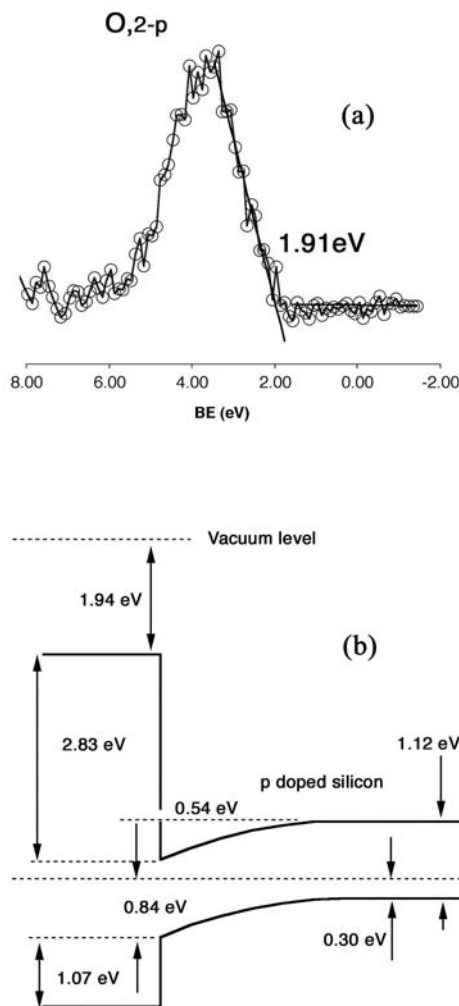Phone: (865) 574-514, Fax: (865) 574-7659, E-mail: mckeera@ornl.gov

Figure 1. Ba-Sr-O/Si Valence Band Edge and Band Diagram. The valence band spectrum is shown in (a) with the oxygen 2-p valence band edge displaced 1.91 eV from the Fermi level of the system. The energy-band diagram in (b) showing valence band (1.91 eV)and conduction band (2.83 eV) offsets for 6 atomic layers of Ba-Sr-O on (001) p-doped silicon assuming the oxide band gap is 5 eV.
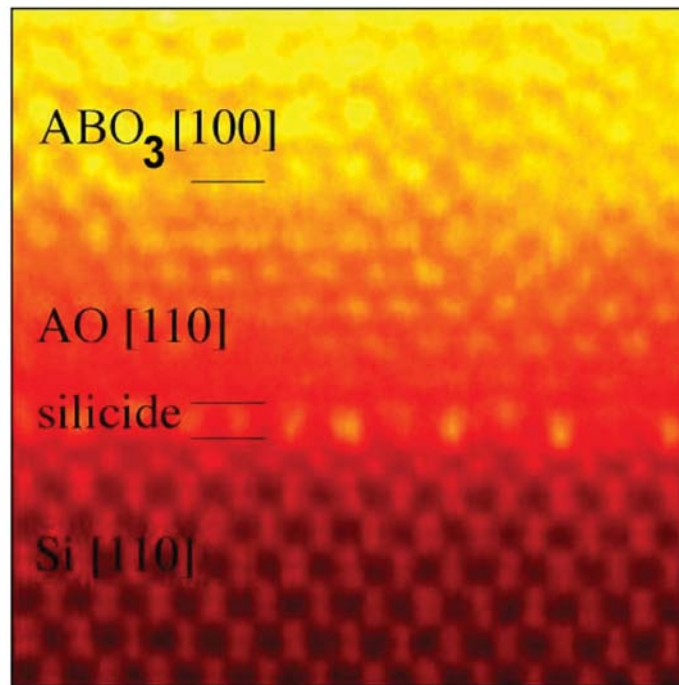

Figure 2. Z-contrast image of crystalline oxides on silicon (COS). The oxide/semiconductor system is stable based on a layer sequencing in which an alkaline earth silicide remains as an interface phase that buffers the electrostatics between the two materials.

Local Conductivity and Defect Annealing in Passive Oxides on Aluminum - Impact on Localized Corrosion

Kevin R. Zavadil and *John P. Sullivan,* Sandia National Laboratories
Chett Boxley and *Henry S. White,* University of Utah
Patrick J. Pinhero, Idaho National Engineering & Environmental Laboratory

Motivation—The stability of Al in an aqueous environment is attributed to the presence of a passivating or barrier-layer oxide on the metal surface. Localized corrosion or pitting is postulated to result from local variations in defect type and concentration in this ultra-thin, 3 to 5 nm thick oxide. Establishing a correlation between highly defective regions of the oxide and regions where pitting is most likely to occur is extremely difficult because no characteristic signatures have been experimentally linked to sites that are most susceptible toward pitting. In addition, pitting results in site destruction preventing post analysis. One potential signature that could be associated with pitting is the local electrical conductivity of the oxide. Identifying the oxide properties responsible for metal stability is an essential component for determining a complete mechanism of localized corrosion.

Accomplishment—A relationship between local conductivity and film stability has been established in a model passivated Al system. Aluminum thin films are deposited using electron beam evaporation resulting in a nanocrystalline films with grains of nominal 150 nm diameters. These films are terminated with a 4.5 nm plasma-formed oxide. A low density of protruding grains exist (see Figure 1a) whose density can be controlled by the deposition rate. Ensembles of these grains can be imaged using atomic force microscopy (AFM) as seen in Figure 1b. These same structures are visible in current sensing AFM (C-AFM) where current is induced between a 0.2 Volt biased AFM tip and the Al sample, as seen in Figure 1c. Electrochemical measurements show that films that possess high densities of these protruding grains also exhibit a high frequency of metastable pitting events when the potential of

the aluminum film is shifted from its equilibrium value in a dilute aqueous chloride solution, as seen in the data of Figure 2a. This film also exhibits significant instability as measured by the potential required to initiate stable pitting (pitting potential). This potential is very narrowly distributed and appears at a lower average value relative to a solution formed oxide on high purity Al, as seen in Figure 2b.

These conductive defect sites are eliminated with longer periods of equilibration of the oxide in solution. The polarization data of Figure 2a show that the meta-stable activity is eliminated by increasing the equilibration time from 1 to 10 hours. In addition, the pitting potential exhibits a broader distribution shifted to higher magnitude indicating a film stability increase. C-AFM measurements show that the density of these conductive sites markedly decreases with increased time of solution exposure. These results demonstrate that the defects in the oxide responsible for meta-stable pitting are annealed with solution exposure.

Significance—Our results show that local variation in oxide conductivity can generate system instability and lower the threshold for pitting corrosion. We have demonstrated this relationship in a tailored oxide but expect similar relationships in alloy systems where the local conductivity variation is driven by differences in the oxide on the alloy matrix and intermetallic particles or by incorporation of alloy constituents into the oxide. Current research is focused on using this experimental approach to spatially resolve and quantify the time-dependent electrical properties of the oxide on bulk Al and candidate alloys.

Contact: Kevin R. Zavadil, Sandia National Laboratories
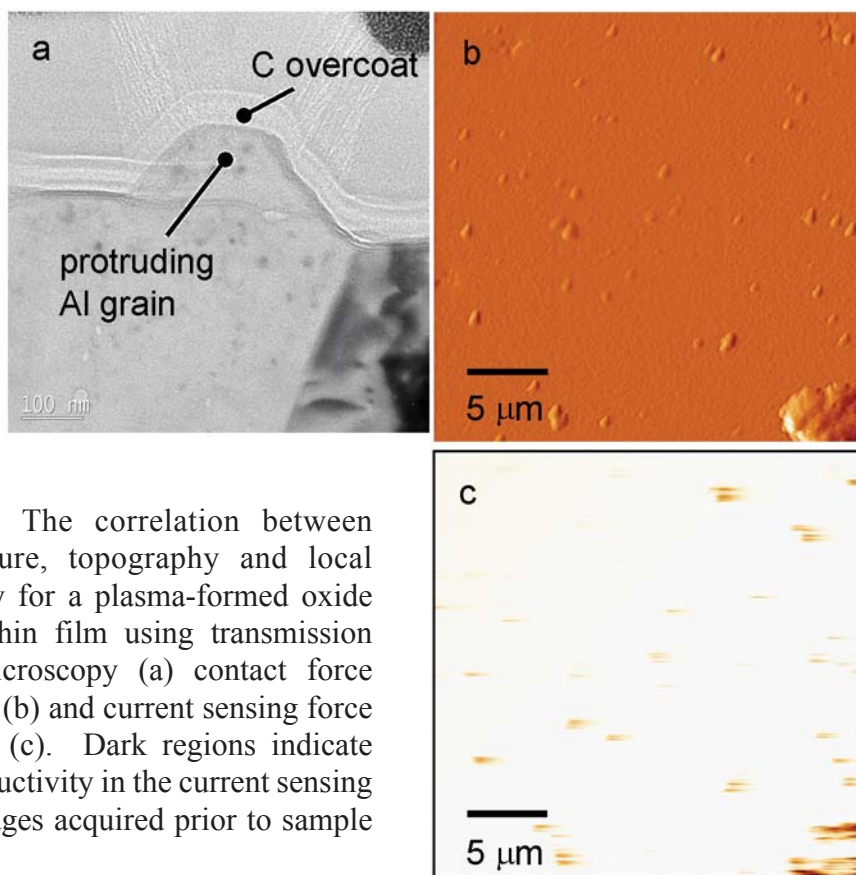Phone: (505) 845-8442, Fax: (505) 844-7910, E-mail: krzavad@sandia.gov

Figure 1. The correlation between microstructure, topography and local conductivity for a plasma-formed oxide on an Al thin film using transmission electron microscopy (a) contact force microscopy (b) and current sensing force microscopy (c). Dark regions indicate higher conductivity in the current sensing image. Images acquired prior to sample immersion.
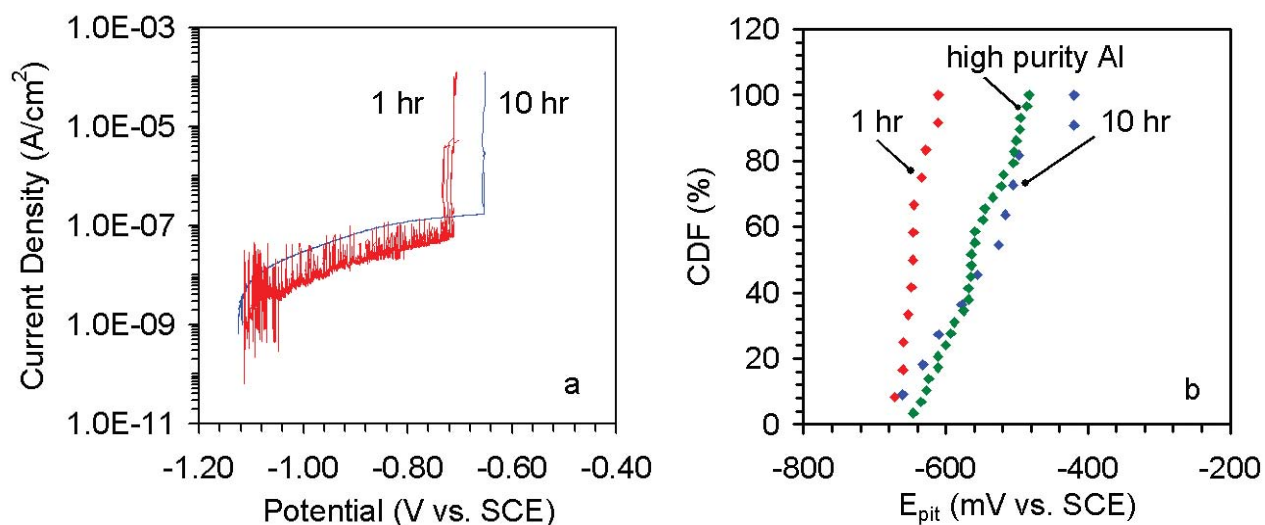

Figure 2. The effect of solution equilibration on the polarization response (a) and the distribution of the pitting potential (b) of a plasma-formed oxide exhibiting an initial high density of conductive sites. The CDF is the cumulative distribution function and the high purity Al data were generated using electropolished 99.99% Al wires.

Kinetic Monte Carlo Modeling of the Aluminum Pit Growth

R. G. Kelly and *M. Neurock,* University of Virginia
H. Isaacs, Brookhaven National Laboratory

Motivation—The physical scales of the important processes that control pitting corrosion range from the atomistic to millimeters. We are attempting to develop computational models at each of the appropriate size scales and then link them together to provide insights into the controlling processes as well as providing connections to other experimental work in this CSP project.

Accomplishment—As part of our multi-scale approach to modeling of the important processes, we have developed a three-dimensional Kinetic Monte Carlo (KMC) model to examine the early development of corrosion pits in metals. It represents a significantly more detailed and realistic set of chemical paths and atomic transformations than included in previous models. It combines the detailed chemistry outlined by Meakin[1] along with three-dimensional modeling of the pit as taken by Sieradzski[2] and Nagatani[3]. It further expands on the detailed chemistry outlined by Meakin[1] and Johnsen[4] by now including water reduction steps along with a set of chemical paths that lead to salt formation within the pit. These two processes make significant contributions to the stability of localized corrosion sites. The UVa KMC method includes a description of the local environment and its effect on the chemical transformations. The effects of local pH, atomic structure (bonding), and concentration of other species are taken into account via effects on the rate constants of the ten reactions considered. Figure 1 shows a progression of a pit in one simulation. Other than the initial condition, only the interior surface atoms of the pit are shown (*i.e.*, unoxidized Al atoms are removed for clarity in Figure 1b-e). The irregular nature and lateral spreading of the pit surface qualitatively reproduces what is seen experimentally in larger samples. The recent achievement of STM imaging of nm-size pits by Maurice[5] provides the path to make direct comparisons between atomistic pitting models and physical measurements. Figure 2 shows that increasing the strength of the nearest-neighbor interactions on the resulting dissolution front leads to more of a tunneling attack, limiting the lateral attack. The model allows computation of species concentrations and fluxes of different intermediates. These results will feed into our continuum level mass-transport models.

Significance—We have developed a general purpose modeling tool that provides information concerning the initial stages of pitting beyond that of existing models. It generates important chemical and physical information about a pit including local chemistry, shape factor, and instantaneous propagation velocity. Lateral propagation of a pit, as observed in practice, is reproduced by this model. The shape factor can be affected by the degree to which the number of nearest neighbors affects the activation energy for dissolution. We are now poised to use this tool to investigate deterministic factors that control pitting including alloying elements (such as Cu and Mg), bulk solution composition, and electrochemical potential.

[1]Meakin, P., T. Jossang, and J. Feder, Phys. Rev. E, 48, 4, 1993, 2906-2916

[2]Erlebacher, J., M.J. Aziz, A. Karma, N. Dimitrov, and K. Sieradzki, Nature, 410, 2001, 450-453

[3]T. Nagatani, Phys. Rev. Lett., 68, 10, 1992, 1616-1619

[4]Johnsen, T., and R. Hilfer, Phys. Rev. E, 55, 5, 1997, 5433-5442

[5]V. Maurice, L. H. Klein, and P. Marcus, *Electrochemical and Solid-State Letters,* 4 (1) B1-B3 (2001)

Contact: Robert G. Kelly, University of Virginia
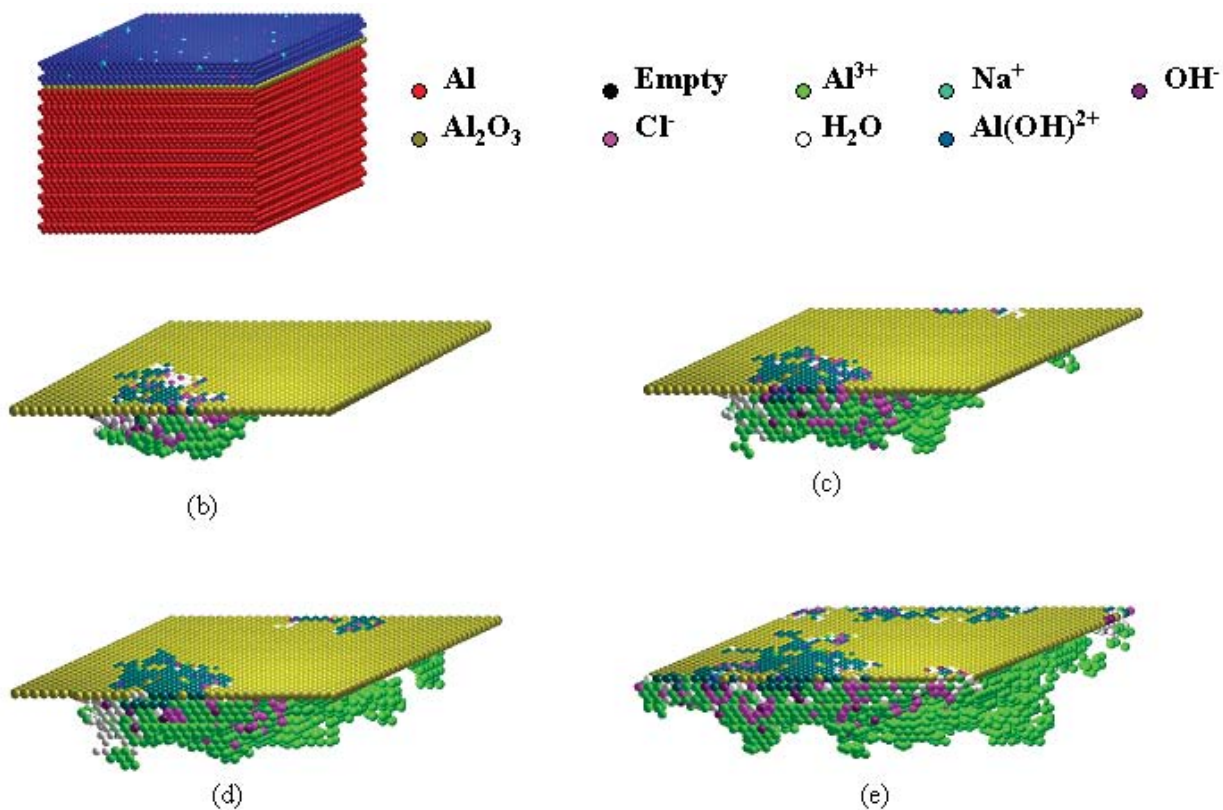Phone: (804) 982-5783, Fax: (804) 982-5799, E-mail: rgkelly@virginia.edu

Figure 1. Initial 3-D lattice representing Al single crystal (111) orientation to solution. (a) 10,000 time steps after initiation of pit, (b) 30,000 time steps, note that growth of pit on rear edge is continuation of original pit as periodic boundary conditions are used, (c) 50,000 time steps, (d) 90,000 time steps.
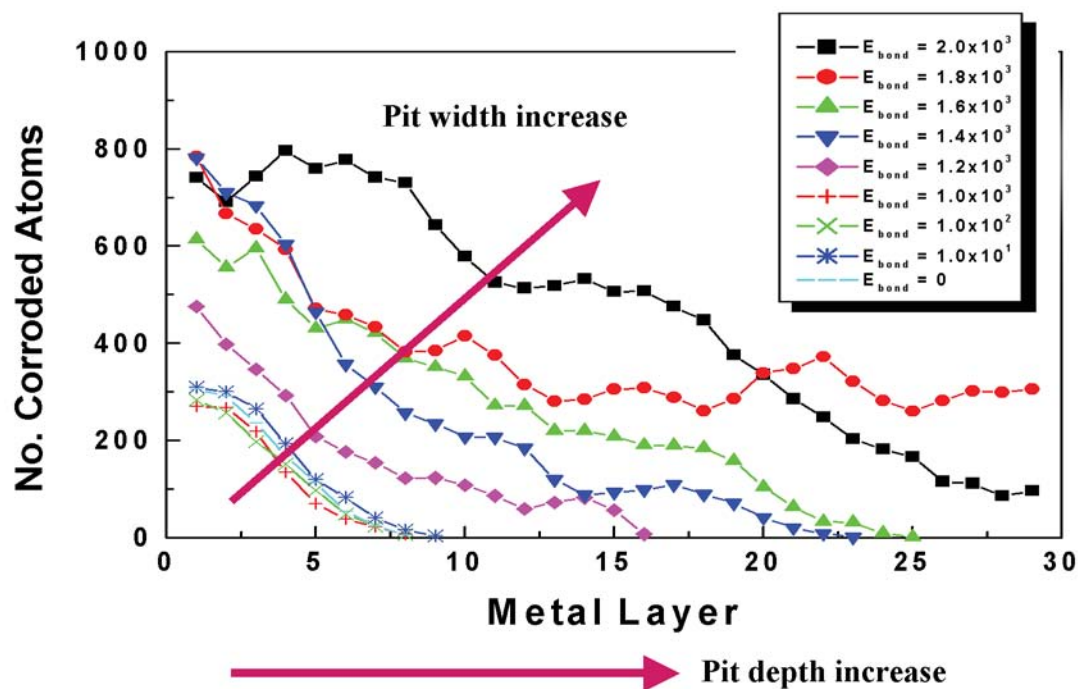

Figure 2. Number of corroded atoms in each atom plane as a function of the strength of the nearest-neighbor interaction term (E_{bound}) on dissolution activation energy after 250,000 time steps.

The Use of Bulk and Thin Film Solid Solution Analogs for Studies of Al Alloy Corrosion

C. F. Windisch Jr., D. R. Baer, M. H. Engelhard, and *R. H. Jones,*
Pacific Northwest National Laboratory
R. G. Buchheit and *Y. Kim, Ohio State University*

Motivation—. This CSP project has the objective to determine the metallurgical factors in localized corrosion and stress corrosion cracking and ask the central motivating question:

"What is the role of alloying element segregation and precipitation on localized corrosion phenomena?"

We are currently focused on understanding the role of Cu and, to a lesser extent, Mg and Zn on Al alloy corrosion processes. Our research strategy has been to study the isolated phenomena with the following materials and techniques:

- Bulk and thin film phase pure analogs
- Specially designed alloys
- Manufactured microstructures
- Small length scale probes
- Combined electrochemistry and surface analysis

Accomplishment—Studies were performed in NaCl solutions at both pH = 10 and at neutral pH. The former provided information regarding the effects of Cu on Al alloy corrosion in the absence of a protective film such as would exist at a crack tip. The latter determined the influence of Cu on localized corrosion, including pitting, when a passive film is present.

As shown in Fig. 1, application of an anodic potential to Al-Cu alloys in NaCl solution at pH = 10 initially gave rise to anodic (negative) currents associated with corrosion, but then the currents became cathodic (positive) with the amount of cathodic current greater at higher Cu contents. XPS depth profiles of Al-Cu samples treated in this way (Fig. 2) showed that the Al was selectively oxidized and a layer of Cu accumulated at the metal/oxide interface. Open circuit potentials of the Al-Cu samples (and Mg-containing alloys as well) scaled with the reversible potentials of the alloys calculated from the reversible potentials of the constituent metals and their composition (Fig. 3). These results indicate that, in the absence of a passive film, Al corrosion is enhanced by the presence of Cu through a selective dealloying process. Studies at neutral pH using a microelectrode array showed that Cu increases the pitting potential of Al (Fig. 4) as well as the distribution of pitting potentials over the metal surface (Fig. 5). The latter result was particularly apparent when the potential was held just below the pitting potential for several minutes, allowing the passive film to become thicker and/or defects to heal.

Significance—The results suggest that the role of Cu in the corrosion of Al-Cu alloys differs depending on whether a passive film is present on the metal or not. If a passive film is not present, Cu may promote corrosion through selective oxidation of the Al, whereas, if a passive film is present, Cu appears to inhibit localized corrosion by changing the characteristics of the passive film.

Contact: Chuck Windisch, Pacific Northwest National Laboratory
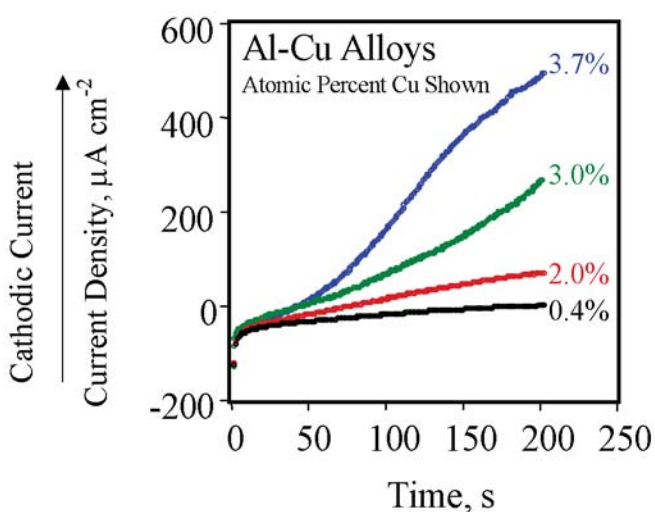Phone: (509) 375-6538, Fax: (509) 375-2186, E-mail: cf.windisch@pnl.gov

Figure 1. Variation of current density after applying +100 mV (vs. OCP) step to Al-Cu alloys in 3.5% NaCl solution at pH = 10.
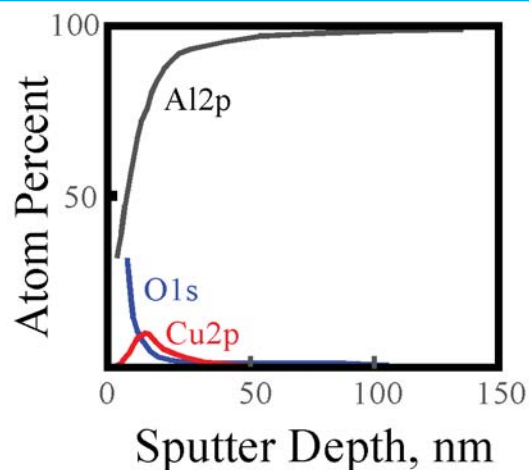

Figure 2. XPS depth profiles of corrosion film on Cu-implanted Al sample 500s after potential step to +100 mV anodic of the original open-circuit potential.
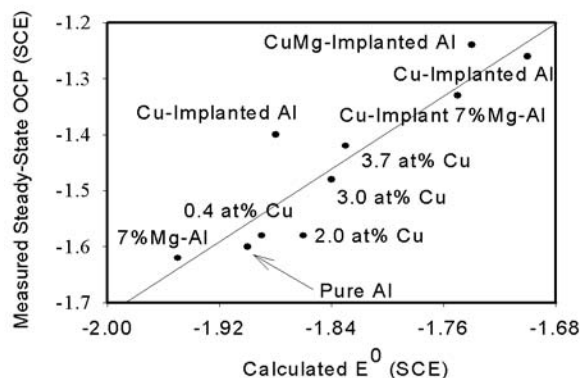

Figure 3. Variation of measured open-circuit potentials of various Al alloy compositions in 3.5% NaCl at pH = 10 vs. reversible potentials calculated from metal constituents.
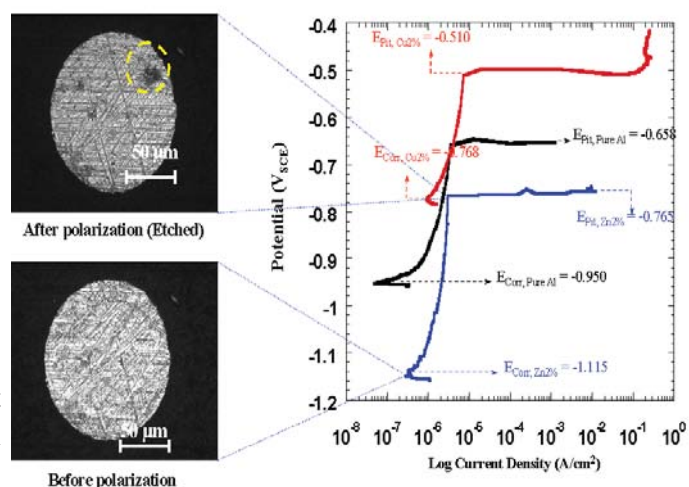

Figure 4. Polarization curves for pure Al and Al alloys showing shift of pitting potential to more noble potentials when Cu is present.
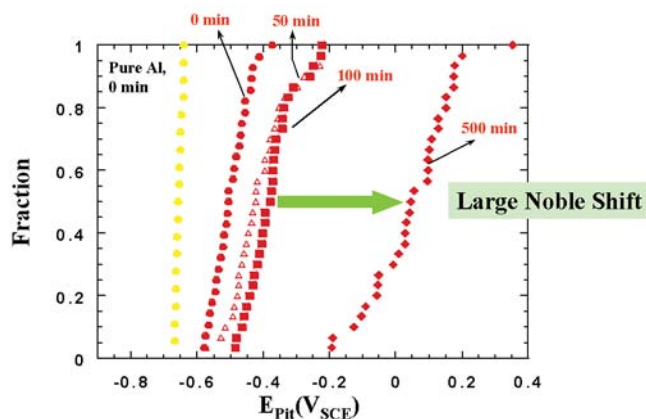

Figure 5. Distribution of pitting potentials for pure Al (yellow) and Al-2%Cu after holding for various times below the pitting potential.

Identifying Stress-Induced Nanocracks in YBa$_2$Cu$_3$O$_7$ Coated-Conductors Due to Oxygen Diffusion Through Sol-Gel Buffer Layers into Ni(100) Substrates

M. Siegal, P. Clem and *J. Dawley, Sandia National Laboratories*
S. Folytn and *T. Holesinger, Los Alamos National Laboratory*

Motivation—The development of YBCO (YBa$_2$Cu$_3$O$_{7-\delta}$) coated conductors is promising for the fabrication of superconducting tape for magnet and electric power applications. High current density YBCO can grow onto biaxially-textured metal tape, such as Ni(100), using high-ly-oriented metal-oxide buffer layers. The buffers must provide a lattice-matched template for epitaxial YBCO growth and a diffusion barrier to prevent Ni(100) oxidation during the YBCO growth. While typically grown using high-vacuum deposition processes, low-cost chemical solution methods show great promise. Sandia recently reported the first high-current coated-conductor fabricated solely using sol-gel for all layers. The buffer is highly-oriented STO (SrTiO$_3$) grown onto Ni(100). The use of STO buffer layers is exciting due to its superb lattice match and chemical compatibility with YBCO. However, as improvements in STO orientation and morphology were made, current-carrying properties were lost. We want to know why.

Accomplishment—STO buffer layers, 200-nm-thick, grow via sol-gel methods onto Ni(100) tape using a template layer of either (Ba,Sr)TiO$_3$ (BST) or BaCaTiO$_3$ (BCT). BST and BCT grow with near-perfect orientation onto Ni(100). STO grain size is controlled by a combination of growth temperature and choice of solvent solutions. Large grains of oriented STO, seemingly a more ideal template for YBCO growth than smaller grains, also lead to greater intergranular porosity. However, such buffers do result in highly-oriented YBCO films. Fig. 1(a) shows the x-ray diffraction (XRD) pattern of a 1.3-μm-thick YBCO layer grown using pulsed-laser deposition (PLD). This predomi-nantly c-axis YBCO film with a transition tem-perature T$_c$ = 87 K, also has a significant NiO

diffraction peak. This film carries very little supercurrent. Fig. 1(b), a transmission electron microscopy (TEM) image, finds nm-sized cracks in the YBCO layer.

Similar TEM results, shown in fig. 2(a), from a 100-nm-thick YBCO film grown using sol-gel helps explain the nature of the nanocracking, which appears only after exposing the buffered-Ni(100) to the oxidizing conditions of the YBCO growth process. Nanocracks are again observed in the YBCO layer. Interestingly, we also identify the formation of a nonuniformly-thick layer of NiO at the Ni-buffer interface. X-ray spectral image analysis performed in the boxed region, shown in fig. 2(b), confirms the presence of NiO, as well as protrusion of NiO into the STO buffer layer grain boundaries and pores. Positive identification of NiO at the buffer/substrate interface from either PLD or sol-gel YBCO growth suggests that it results from the oxidizing conditions of YBCO growth. The existence of this NiO layer, with very dif-ferent thermal expansion coefficients from the other materials present, can result in stresses that easily lead to the observed YBCO nanocracking.

Significance—Nanocracks are unacceptable defects in superconductors since they prevent supercurrent flow. By confirming the existence of both nanocracks and NiO formation from two completely different YBCO growth processes, we conclude that 200-nm-thick STO buffer lay-ers do not sufficiently prevent oxygen diffusion. Further improvements are required to take advantage of the superb template properties of STO. Recent studies find that somewhat thicker STO layers can limit oxygen diffusion into the substrate, and pathways now exist for solving this critical materials issue.

Contact: Michael P. Siegal, Sandia National Laboratories
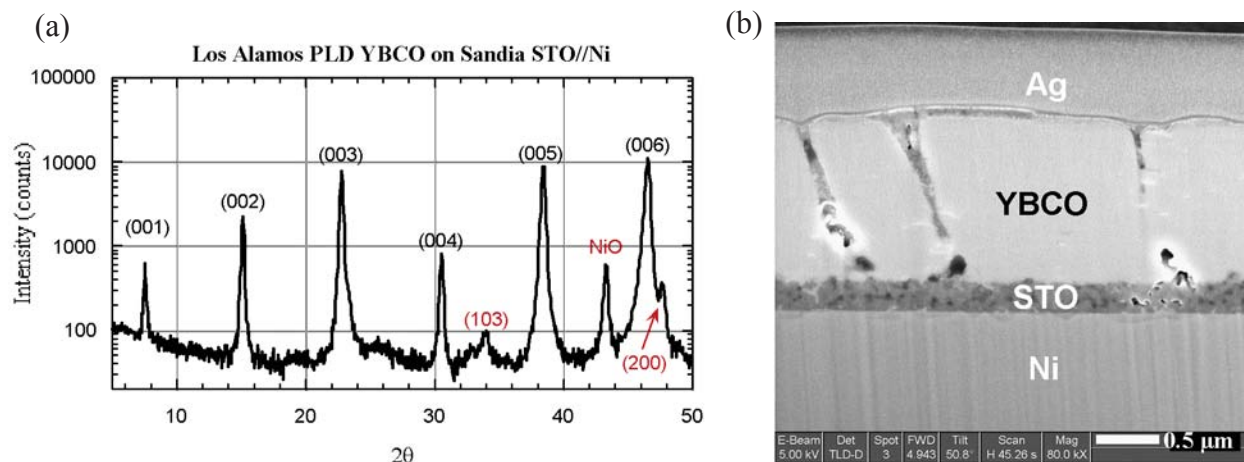Phone: (505) 845-9453, Fax: (505) 844-4045, Email: mpsiega@sandia.gov

Figure 1. (a) X-ray diffraction pattern shows the predominant c-axis (00l) alignment of a 1.3-μm-thick YBCO film grown by PLD onto a sol-gel BST-templated STO-buffered Ni(100) substrate, and the presence of significant NiO formation. (b) Cross-sectional TEM shows the existence of nanocracks in the YBCO layer.
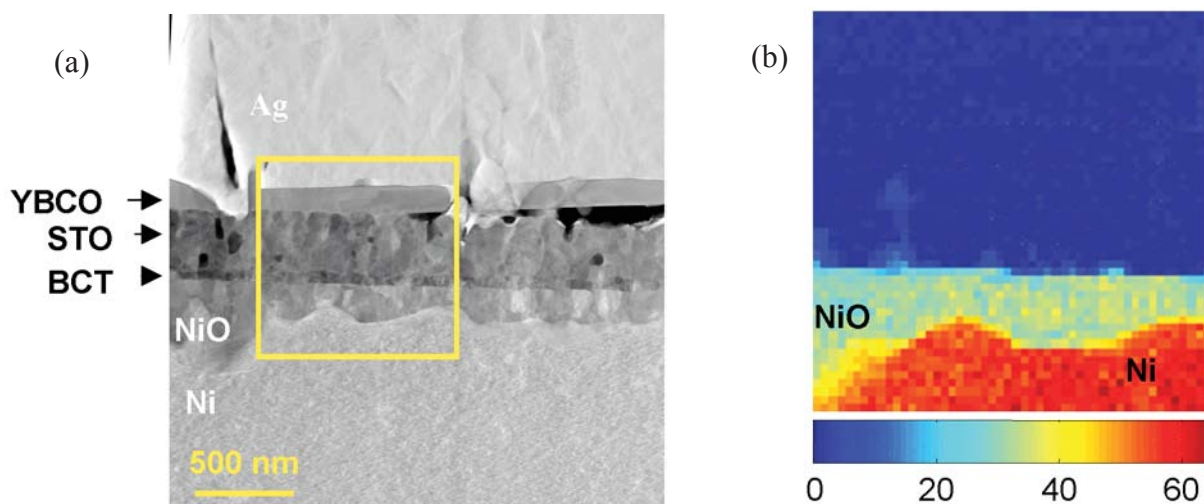

Figure 2. (a) Cross-sectional TEM image of YBCO/STO/BCT/Ni(100) prepared by focussed ion beam (FIB) milling. Each layer is well-defined, however voids appear in the YBCO layer which correspond to nanocracks. Beneath the BCT template layer is a rough layer of NiO. (b) X-ray spectral analysis taken from the 1 square micron inset in (a) confirms that this nonuniform layer at the buffer/Ni interface is NiO, and that some NiO protrudes upward into the STO buffer layers, most likely through grain boundaries and porous voids.

Growth Morphology and Microstructure of YBa$_2$Cu$_3$O$_7$ on Inclined-Substrate-Deposited MgO Coated Conductor Templates with LaMnO$_3$ Buffer Layers

Beihai Ma, D. J. Miller, and *Balu Balachandran, Argonne National Laboratory*
T. Aytug, J. D. Budai, D. K. Christen, P. Paranthaman, and *R. Feenstra,*
Oak Ridge National Laboratory

Motivation—New "coated conductor" approaches to fabricating high-temperature superconductor (HTS) wires are under development as a means to overcome the problem of "weak-link" current transport across high-angle grain boundaries in cuprate superconductors. A crucial component of these tape-like conductors is the textured buffer layer(s) that serve to provide a crystalline template for epitaxial growth of the HTS, while avoiding chemical contamination by the underlying metal tape. Of the three principal approaches to coated conductors, Inclined Substrate Deposition (ISD) is conceptually and practically the simplest, and potentially most cost-effective. This method, being pursued at ANL, achieves biaxial crystalline texture of MgO through a combination of rapid growth mechanisms and self-shadowing that occurs for species incident at a large deposition angle. Remaining issues include the ability to achieve sharp texture, adverse effects of surface roughness, and strong inclination of the principal buffer-layers axes, all of which may impact the quality of the HTS coating. Recently, ORNL has shown that sputtered LaMnO3 (LMO) buffer layers are structurally compatible with both MgO and YBCO, as demonstrated by the high critical current densities achieved in YBCO films grown on model, single crystal systems (see Fig. 1). The present work was aimed at elucidating the structural and superconducting properties of YBCO films grown on LMO buffer layers deposited by ORNL on ISD MgO/Hastelloy tapes made at ANL.

Accomplishment—The ISD MgO was deposited at ANL by electron-beam evaporation to a thickness of a few microns, with the incident flux aligned ~55° from the surface normal, followed by a thin homo-epitaxial layer of MgO to provide improved surface smoothing. Buffer layers of LMO were deposited at ORNL on these substrates by *rf* magnetron sputtering to a thickness of about 250 nm. Subsequently, pulsed laser deposition was used to grow ~200 nm thick YBCO films. Superconducting properties and structural studies by X-ray diffraction and cross-section TEM were conducted, with the results illustrated in Figs. 2 and 3. Overall, it is found that cube-on-cube epitaxial growth occurs throughout the layers, with common [001] (*c*-axes) aligned nominally out-of-plane, and [110] axes in-plane. However, distinctive of the ISD technique, the [001] axes are tilted approximately 36° from the surface normal and toward the original MgO plume. Crystalline structure is well maintained, and the mosaic distribution of grain misorientations is in the range of several degrees FWHM, which are typical texture levels of most coated conductor approaches. Although the YBCO *c*-axis is tilted, the geometry is such that the supercurrents flow in the *a-b* basal planes, as shown in Fig. 3, which is the optimal situation for superconductive transport. In the present study, the achieved critical current density, J$_c$, reached values of 250 kA/cm^2 at 77K, approaching the levels needed for coated conductor applications.

Significance—We have demonstrated large Jc values on a coated conductor prototype using a combination of the ISD texturing approach and the efficacy of a LaMnO$_3$ cap buffer layer. The present results offer promise for the further development of a rapid, cost-effective method to produce high-current coatings on metal tapes for long-length conductors.

Contact: Dean J. Miller, Argonne National Laboratory
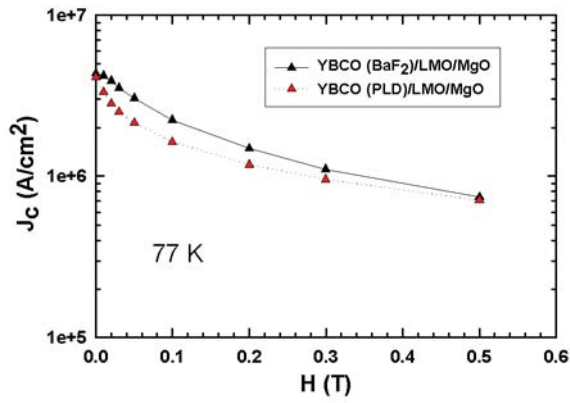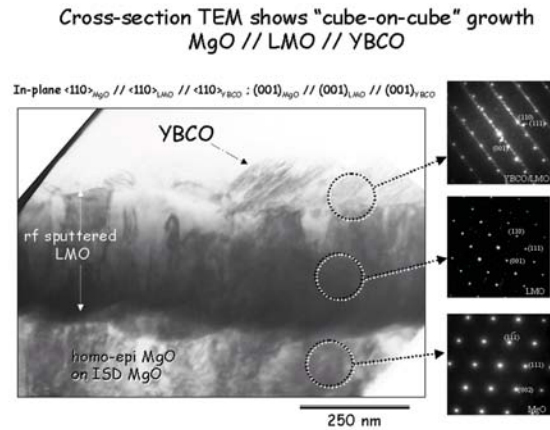Phone: (630) 252-4108, Fax: (630) 252-4289, Email: miller@anl.gov

Figure 1. The critical current density at 77 K as a function of magnetic field for YBCO films deposited on LMO-buffered MgO single crystals. The data for these model systems show excellent properties and demonstrate the compatibility of sputtered LMO buffer layers with MgO substrates and YBCO coatings.

Figure 2. *(a)* A schematic of the ISD approach, and X-ray θ–2θ scans that show the LMO and YBCO are epitaxially aligned, with the cube axis tilted about 36° from the surface normal. *(b)* X-ray pole figures of the YBCO (006) + (020) and (115) reflections illustrate the level of grain texture, with misalignment distributions of a few degrees FWHM.
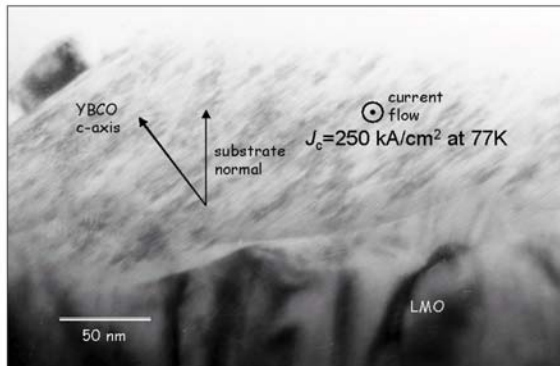

Figure 3. TEM cross-section images and selected area electron diffraction confirm the microstructural integrity and cube-on-cube growth of LMO on MgO, and the direct epitaxy of YBCO, which results in a ~36° tilt of the YBCO c-axis away from the surface normal.
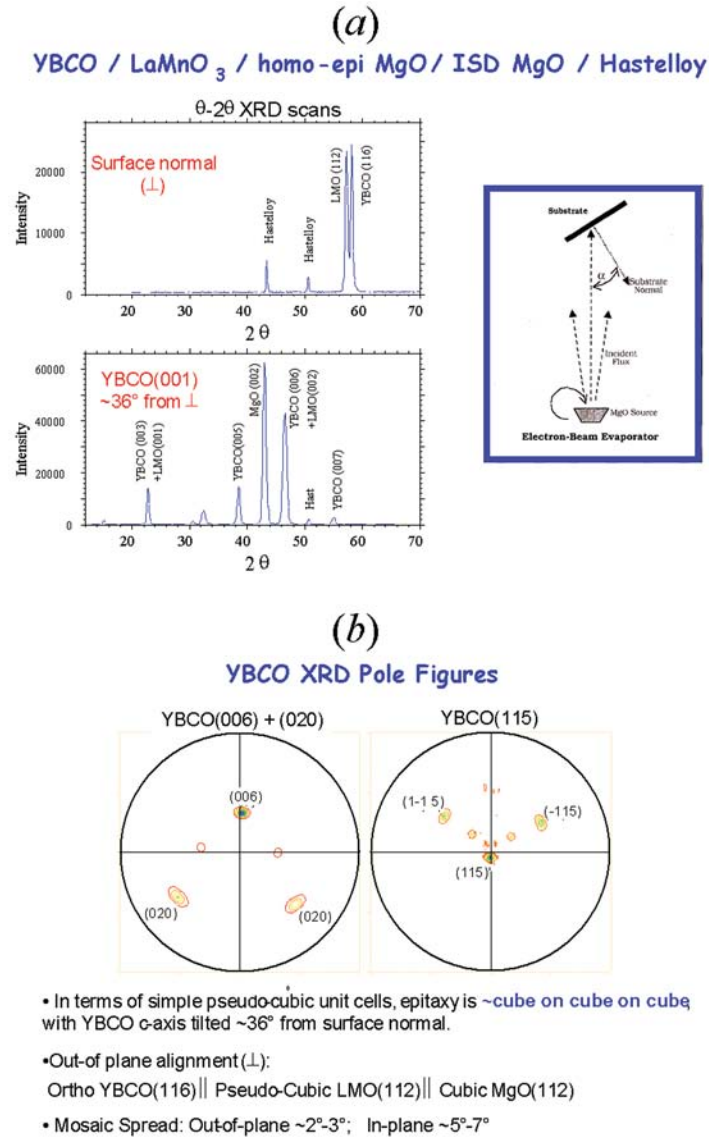
Effect of Oxygen Content on High-T_c Grain Boundaries

B. W. Veal, H. Claus, A. P. Paulikas and **K. E. Gray,** *Argonne National Laboratory*
D. O. Welch and **Haibin Su,** *Brookhaven National Laboratory*

Motivation—The value of kilometer-length coated conductors of textured polycrystalline thick films of high-T_c superconducting cuprates such as $YBa_2Cu_3O_x$ (YBCO) depends on the elimination or amelioration of weak-link behavior in the grain boundaries. The super-current capacity, J_c, of [001] tilt boundaries decays exponentially with misorientation angle beyond ~2 degrees; however, doping with Ca has been shown to improve J_c. Our general goal is to understand grain boundary properties in terms of the interplay between elastic strain, the oxygen content and degree of order, the segregation of dopants, and the formation of space charges at interfaces and dislocation cores.

Accomplishment—We report the effects of oxygen content on the grain boundary J_c. The data of Fig. 1 show a systematic improvement in J_c with increased oxygen that extends past the optimal doping (maximum T_c) of the grains. This result, which is found for both bulk and thin-film grain boundaries, implies that oxygen affects Josephson coupling by changes in grain-boundary microstructure *in addition to* the known dependence on the strength of superconductivity in the grains. The effect of oxygen doping beyond the optimum T_c exhibits similarities to Ca doping, which lowers the bulk T_c while improving the grain boundary J_c. Our result further implies that optimum grain boundary performance may require separate oxygenation protocols for the grains and the grain boundaries. In addition, our preliminary studies indicate that the oxygen processing protocol is affected by cation dopants, e.g., Ca. To help gain an understanding of which microstructure feature most strongly affects J_c, we have begun a theoretical study based on shell-model interatomic interaction potentials. These potentials were used in atomistic simulations to estimate the energetics of oxygen content and oxygen order in strained lattices such as might occur near dislocations and grain boundaries. Figure 2 shows the energy required for an elementary disordering event in YBCO- the formation of a vacant oxygen chain site (O_1) accompanied by an oxygen ion placed on a normally empty chain site (O_5)-as a function of strain, caused by stress or by "chemical pressure" due to, e.g., replacing Y cations by rare-earth cations or Ba cations by alkaline-earth cations. It is seen that stress and "chemical pressure" can substantially alter the ease of formation of disorder. Statistical thermodynamic models including elastic strain are used to estimate the equilibrium oxygen content and state of disorder near edge dislocations in tilt boundaries. The results show that significant changes of oxygen content and enhancement of oxygen disorder in regions of tensile strain are induced by elastic fields near the dislocations.

Significance—The relative roles of strain and space charge as the source of the depression of the critical current density (by [001] tilt boundaries) in YBCO have been actively debated. Our research suggests that oxygen content, strain and oxygen disorder have very important effects. Detailed modeling of the combined effects of elastic strain fields, chemistry and disorder may provide a key to understanding and ameliorating this important aspect of grain boundary behavior in cuprates.

Contact: D. O. Welch, Brookhaven National Laboratory
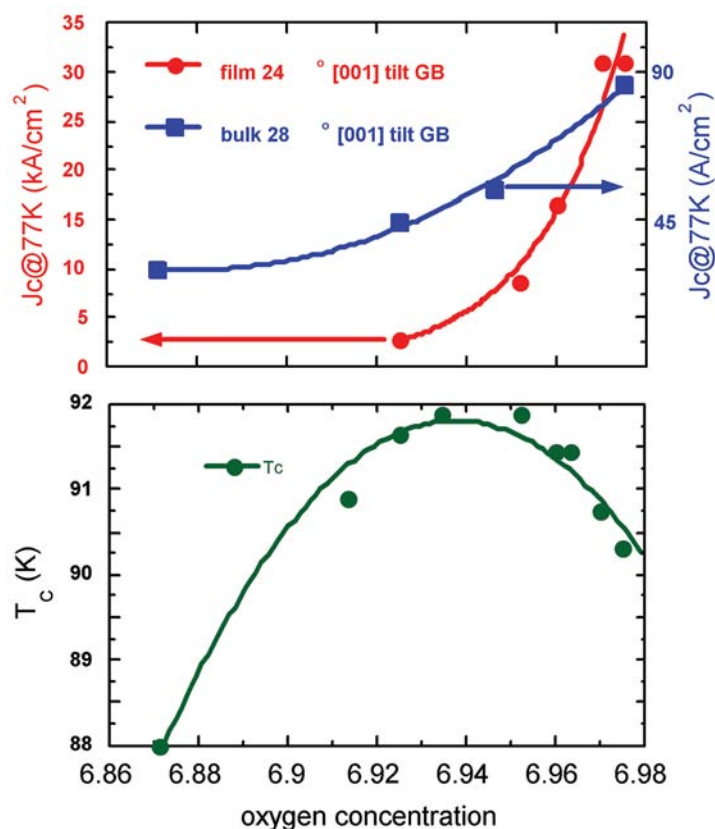Phone: (631) 344-3517, Fax: (631) 344-4071, E-mail: dwelch@bnl.gov

Figure 1. As a function of oxygen concentration, the grain boundary J_c of YBCO films and bulk, shown here at 77 K, continues to increase even as T_c drops in the overdoped regime of the grains (>6.94). The effect is especially large for films.
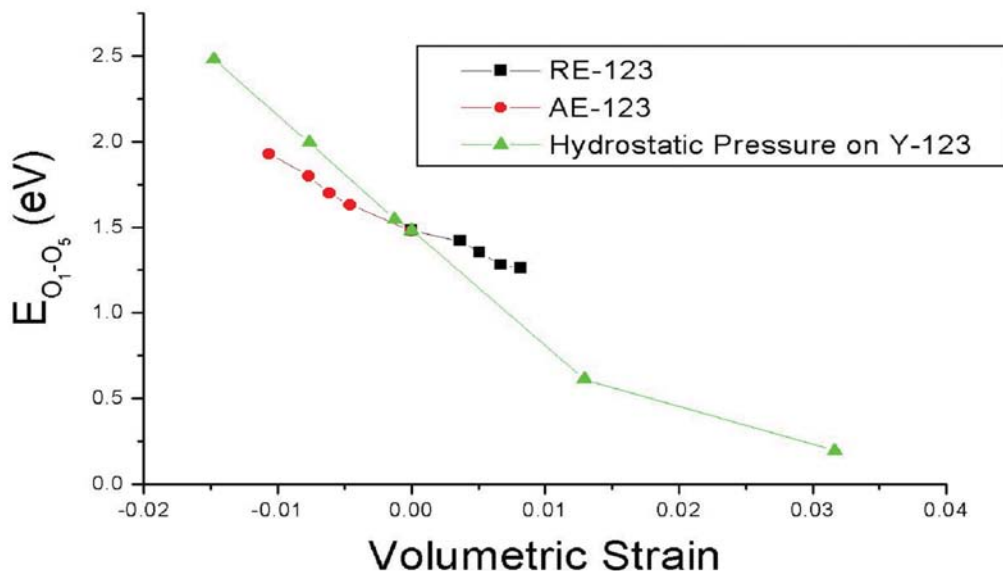

Figure 2. The strain dependence, relative to strain-free YBCO, of the elementary event of oxygen disordering in orthorhombic 123 caused by lattice stress from hydrostatic pressure, or by "chemical pressure" resulting from replacing Y by rare-earth cations (RE) or Ba by alkaline earth cations (AE).

In-Situ Nanoindentation of Amorphous Diamond Thin Films in a TEM

Andy Minor and *Eric Stach,* *Lawrence Berkeley National Laboratory*
Tom Friedmann, *Sandia National Laboratories, NM*

Motivation—Amorphous diamond (a-D) thin films have great potential to be used as surface coatings for MEMS devices due to their excellent mechanical properties, low energy surface (reduced stiction), and biocompatibility. The a-D thin films are deposited by pulsed laser deposition from a graphite target and result in highly sp^3-bonded, but amorphous, carbon films with hardness values approximately 80-90% that of crystalline diamond.[1] In order to elucidate the underlying physics of the mechanical deformation process in these materials, we have utilized the new technique of in-situ nanoindentation in a transmission electron microscope (TEM).[2,3]

Accomplishment—In order to perform the *in situ* nanoindentation experiments, the a-D thin films were deposited onto micromachined wedge-shaped silicon substrates with the required geometry for electron transparency as well as mechanical stability during indentation in a TEM. Indentations were performed on the cap of film at the peak of the wedge, which was terminated by a plateau approximately 20 nm in width. A scanning electron micrograph of a cross section from an a-D coated *in situ* sample is shown in Figure 1, where the direction of indentation is indicated. The diamond is mounted on a piezo-ceramic actuator, which both controls its position in 3 dimensions and forces it into the edge of the sample. Since the a-D thin film was considerably harder than the silicon substrate, it was found that the deformation of the film was controlled by the deformation of the underlying substrate. Specifically, the deformation of the a-D thin films was either minimal or nonexistent, and as the indenter penetrated the sample the underlying silicon deformed before any noticeable damage to the a-D thin film. Figure 2 shows bright field, and dark field TEM micrographs of the post indentation microstructure. As can be seen, the silicon sample deformed through dislocation nucleation and propagation, while the a-D thin film showed minimal decrease in thickness even at the point of indentation. The deformation in the underlying silicon was highly localized, and resulted in dimpling of the a-D film with no occurrence of spalling. In fact, the deformation in the underlying substrate is characteristically the same as when the silicon wedges are left uncoated, as reported recently.[4]

Significance—The purpose of a hard surface coating is to protect the underlying material from mechanical and chemical damage. In the case of sharp silicon wedges, we have clearly demonstrated that the a-D thin films do not decohere from the silicon substrate during nanoindentation. These films are deposited by a line-of-sight process and yet they show good coverage on sloped sidewalls - as is demonstrated in the even deposition over the ultra-sharp silicon wedges shown here. Even during nanoindentation, where the stresses underneath the indenter can reach the theoretical strength of the material,[5] the a-D thin films are shown to retain their adherence to the substrate. Thus, we have shown that a micromachined device coated with an a-D film can be expected to retain its superior mechanical and chemical properties even after the application of a large and highly localized stress. Similar studies of ultrananocrystalline diamond thin films are underway, and intial indications are that they too act as effective coatings for MEMS.[6]

Contact: E.A. Stach, Lawrence Berkeley National Laboratory
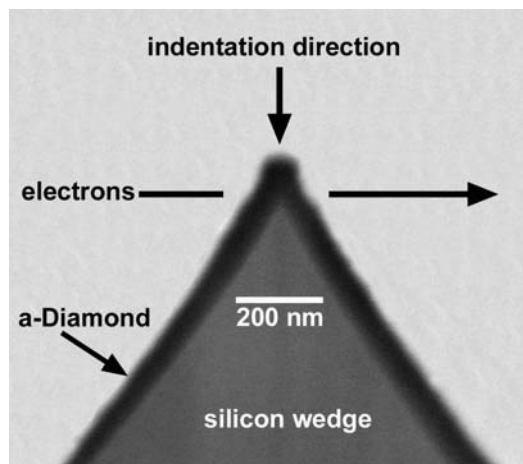Phone: (510) 486-4634, Fax: (510) 486-5888, E-mail: eastach@lbl.gov

Figure 1. Scanning electron micrograph of a lithographically-prepared silicon wedge coated with amorphous diamond in cross-section.
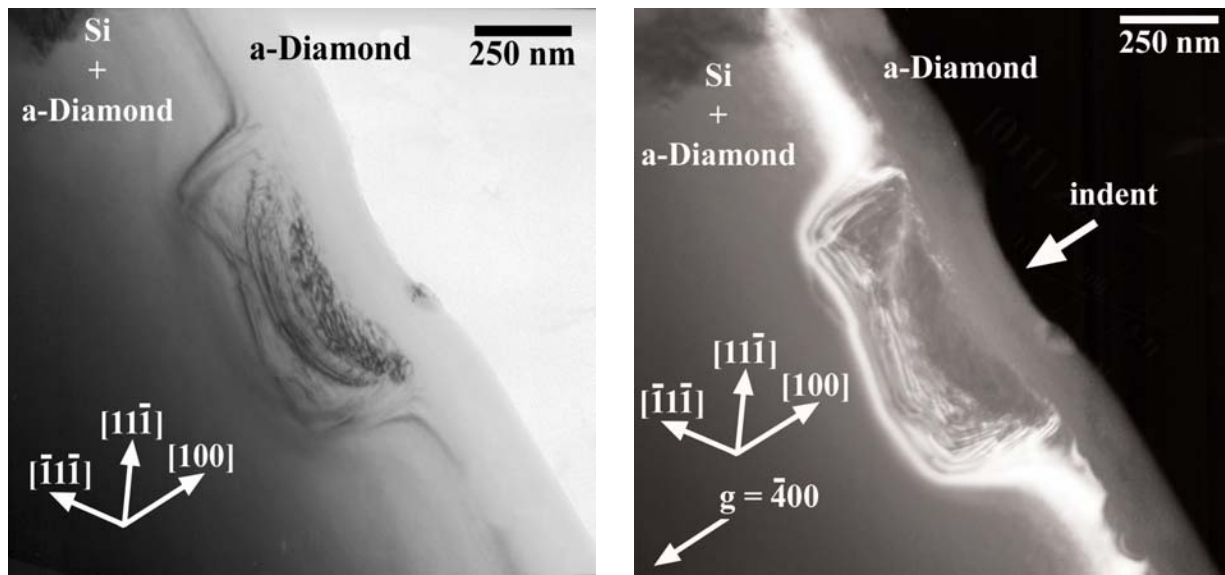

Figure 2. (a) Bright field and (b) dark field TEM micrographs of an indentation of a silicon wedge coated with amorphous diamond. The deformed region in the silicon consists entirely of dislocations and no additional regions consisting of different phases, while the deformation in the amorphous diamond film is minimal or non-existent.

[1]T. A. Friedmann, J. P. Sullivan, J. A. Knapp, D. R. Tallant, D. M. Follstaedt, D. L. Medlin and P. B. Mirkarimi "Thick stress-free amorphous-tetrahedral carbon films with hardness near that of diamond" *Appl Phys Lett*, **71** (26), 1997 p. 3820.
[2]A.M. Minor, J.W. Morris, Jr. and E.A. Stach, "Quantitative *in situ* nanoindentation in an electron microscope" *Appl. Phys. Lett*. **79** (11), 1625-7 (2001).
[3]E.A. Stach, T. Freeman, A.M. Minor, D.K. Owen, J. Cumings, M.A. Wall, T. Chraska, R. Hull, J.W. Morris, Jr., A. Zettl, and U. Dahmen, "Development of a nanoindenter for *in situ* transmission electron microscopy" *Microscopy and Microanalysis*, **7** (6), 507-17, 2001.
[4]A.M. Minor, E.T. Lilleodden, E.A. Stach, and J.W. Morris, Jr., "Room temperature dislocation plasticity in silicon" submitted to *Nature 9/17/01*.
[5]C.R. Krenn, D. Roundy, M.L. Cohen, D.C. Chrzan, and J.W. Morris, Jr., "Connecting atomistic and experimental estimates of ideal strength" *Phys Rev B*, **65**, 2002 p.13411.
[6]D.M. Gruen, "Ultrananocrystalline diamond in the laboratory and the cosmos" *MRS Bulletin* **26** (10) 771-776, 2001.

Growth of (100) Diamond using Dicarbon

M. Sternberg, P. Zapol, L. A. Curtiss, J. A. Carlisle, and *D. M. Gruen,*
Argonne National Laboratory

Motivation—Ultrananocrystalline (UNCD) diamond is a novel material that is grown in hydrogen poor plasmas and is charaterized by a microstructure consisting of crystallites with an average size of 3-10 nm. It has much potential in the areas of microelectromechanical systems, electronics, and biocomposite materials. Computational studies are aimed at understanding the growth mechanism on the (100) surface of diamond as this is believed to be the rate determining step. Understanding the growth mechanism will help in controlling the morphology and conductivity of the films.

Accomplishment—We have used a density-functional based tight-binding method to study diamond growth by depositing C_2 and CN species onto a hydrogen-free diamond (100)-(2 × 1) surface shown in Fig. 1. This is being used to model the growth of UNCD films under hydrogen-poor conditions. In our simulations, we investigated stable adsorbate configurations formed above dimer rows and troughs on the reconstructed (100) surface. In comparing the stabilities of these configurations with well-studied analogues on silicon, a much more complex picture emerges for the structure of ad-dimers on the (100) diamond surface. We have also investigated adsorption and migration barriers using a nudged elastic band (NEB) method.

While initial depositions proceed without barriers into topologically imperfect configurations, lattice site positions are reached only after overcoming barriers of about 1 eV. However, the barriers are slightly lower for clustered adsorbates due to shared strain fields. The migration barriers for ad-dimers are in the range of 2-3 eV and thus significantly higher than adsorption barriers due to relatively large differences in the energies of intermediate local minima. Figure 2 shows a diagram of the potential energy surface for addition of C_2 to a (100) surface. We find viable adsorption pathways leading to chain-growth and step-advancement. However, the barriers suggest that C_2 addition to nohydrogenated dimers would likely lead to new nucleation sites. Comparing our results with previous studies on the (110) surface, we note that deposition barriers are higher and pathways are more complex on the (100) surface.

Significance—These new results on the growth mechanisms of the (100) surface based on C_2 as the growth species indicates that the deposition barriers are higher and pathways are more complex than on the (110) surface. This leads to a strong disparity in growth and re-nucleation rates on the two types of surfaces and help us to understand observed small grain sizes.
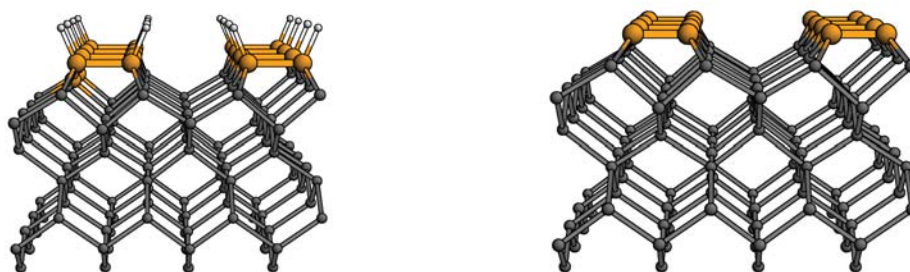
Contact: L. A. Curtiss, Argonne National Laboratory
Phone: (630)-252-7380, Fax: (630)-252-9555, E-mail: curtiss@anl.gov

Figure 1. Illustration of monohydrided 2×1 (100) and nonhydrogenated 2×1 (100) diamond surfaces.

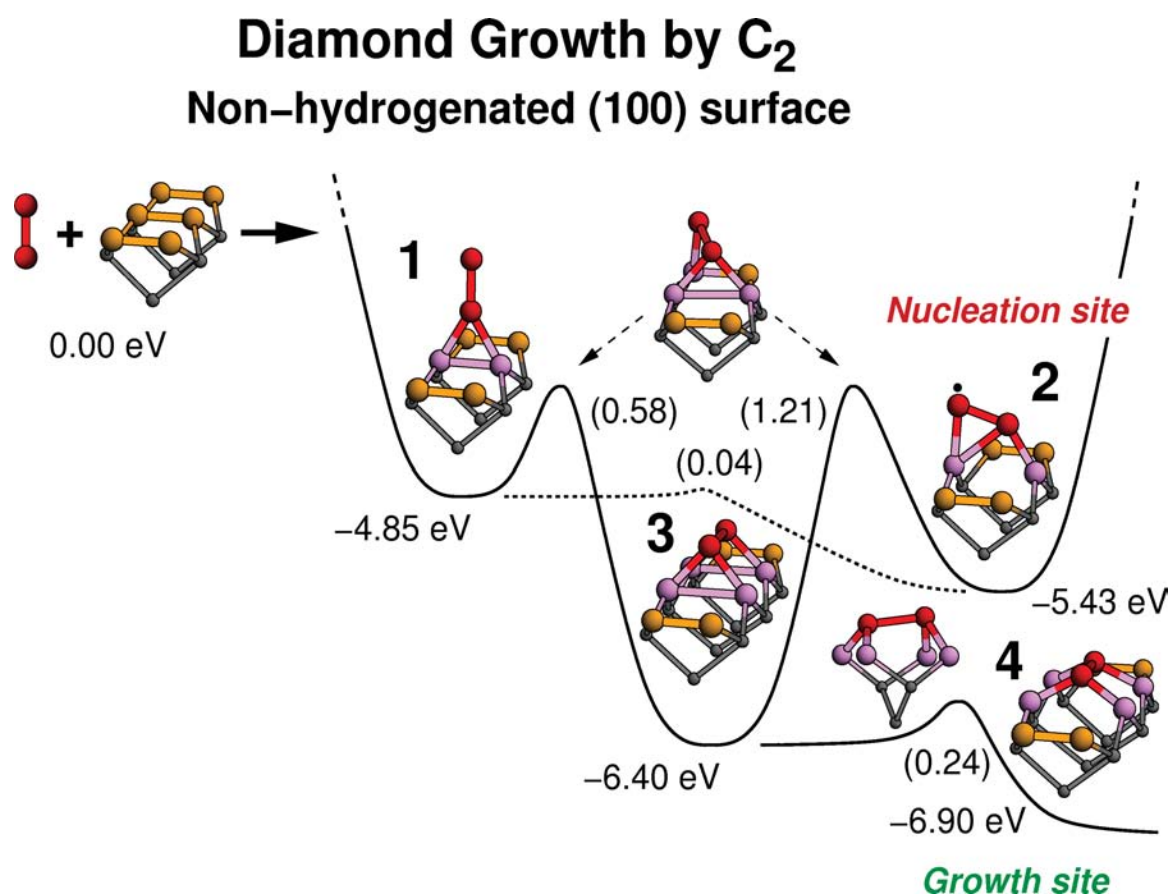
Figure 2. Potential energy surface for addition of C2 to a nonhydrogenated dimer site on the (100) surface. There is a significant barrier (>1 eV) that must be overcome for growth. This probably will result in a high re-nucleation rate.

NMR Bonding Studies of ^{13}C Enriched Amorphous Diamond Films

T. A. Friedmann and *T. M. Alam,* *Sandia National Laboratories, NM*

Motivation—Amorphous diamond (aD) thin films grown by pulsed laser deposition are currently being used in MEMS and sensor technologies. Our discovery that aD thin films can be fully stress relieved has enabled these applications and is a direct result of basic science research on this material. In spite of this research, there is comparatively little understanding of the local bonding structure in these films and the exact nature of the stress relaxation. This is a direct consequence of the fact that both the length and bond angle of 3- and 4-fold bonds can vary considerably. This variability coupled with the amorphous structure make characterization of this material difficult. Useful characterization techniques include Raman spectroscopy, x-ray reflectivity, and electron energy loss spectroscopy (EELS). With these techniques it is possible to infer the mass density and the relative bonding percentage of 3-and 4-fold carbon to within ~5%, but quantitative detailed knowledge of the bonding structure is much more difficult to obtain. NMR spectroscopy of carbon based materials is a well developed field that is capable of probing the local carbon bonding environment quantitatively even in amorphous materials. Unfortunately, it has not been applied to thin film aD samples since no bulk analogue exists, and the NMR signal from unenriched (largely ^{12}C) samples is too small to be useable.

Accomplishment—For the first time, we have been able to grow almost completely enriched (99%) ^{13}C aD samples. The target for the deposition was made by pressing enriched ^{13}C graphite powder to 99% of the theoretical density of graphite. Raman spectra of the enriched samples reveal a large frequency shift due to the heavier ^{13}C atom (Fig. 1) but appear otherwise identical to samples made from unenriched targets. Importantly, we were able to obtain quantitative NMR measurements from these samples. These measurements have been made on as deposited and annealed samples to study the structural changes with annealing that are associated with stress relief (Fig. 2). It is found that the as deposited samples are highly metastable with peaks that are very broad and positions that are shifted due to amorphization from the crystalline analogues of graphite and diamond. Annealing allows for stress relaxation of these bonds and is revealed in the NMR spectra by a peak shift (toward the crystalline) and narrowing of the resonances for both the sp^3 and sp^2 components. Since the peaks are inhomogeneously broadened, this corresponds to an ordering of both bonding types. The high enrichment percentage of this sample also enables the quantitative measurement of correlations between ^{13}C atoms in the sample through the use of 2D RF dipolar recoupling experiments. These experiments have been done and reveal the existence of sp^3 and sp^2 clusters.

Significance—These measurements suggest possible models for the stress relaxation and allow for direct comparison to theoretical structural models derived from first-principles calculations. The relaxation is due to ordering of the two components. This ordering is accompanied by an increase (decrease) in the density of the sp^3 (sp^2) component. Importantly, there is no change in the overall relative percentage of sp^3/sp^2 carbon during this process. Calculations suggest that there is a strong correlation to average bond length (not angle) and the chemical shift suggesting that modification of these strained bonds is the primary relaxation mechanism.

Contact: Thomas A. Friedmann, Sandia National Laboratories, NM
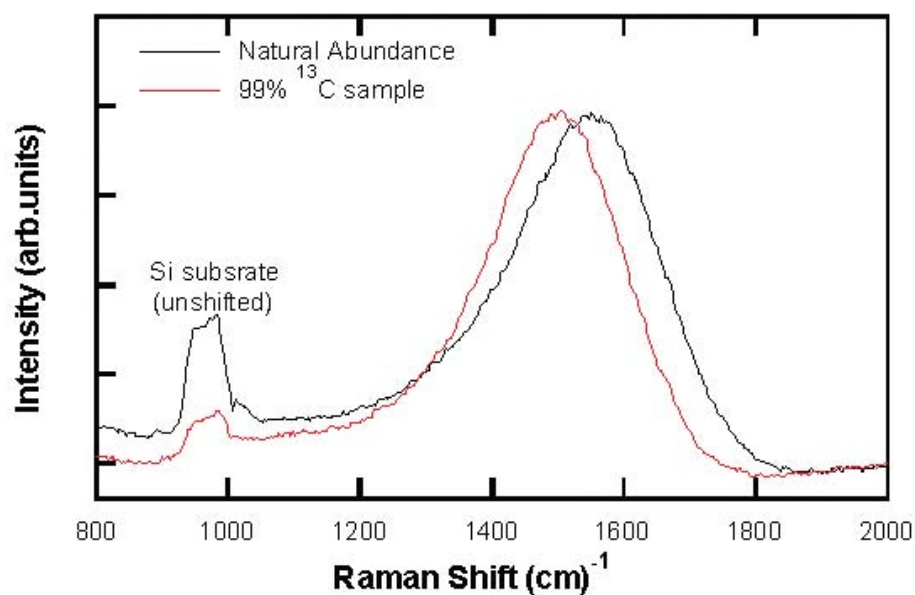Phone: (505) 844-6684, Fax: (505) 844-1197, E-mail: tafried@sandia.gov

Figure 1. Raman spectra of natural abundance and ^{13}C enriched sample. The peak shift is due to the higher mass of ^{13}C vs. ^{12}C.
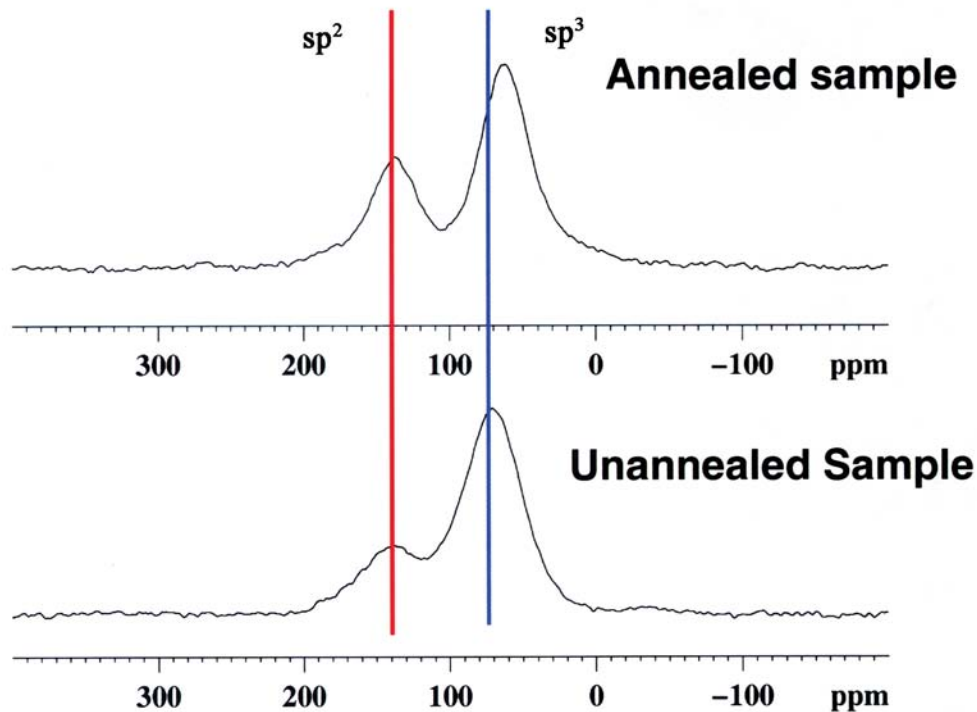

Figure 2. NMR spectra from as-grown and annealed aD films. Both peaks narrow considerably and shift position (especially the sp^3 line) with annealing.

Granular Gases: Theory and Simulations

E. Ben-Naim, *Los Alamos National Laboratory*
S. Y. Chen, *and* **X. Nie,** *Johns Hopkins University*
P .L. Krapivsky, *Boston University*

Motivation—Granular gases consist of macroscopic particles, interacting via hard-core interactions, and dissipating energy via inelastic collisions. With the growing interest in granular material flow and packing came the realization that, even in dilute cases, our theoretical understanding is incomplete. Specifically, granular gases are fundamentally different than classical molecular gases in that non-Maxwellian velocity distributions are observed experimentally. These anomalous statistics are a signature of the existence of strong spatial fluctuations and consequently, significant velocity correlations. Our focus is on studying basic characteristics of freely evolving and driven granular gases using large-scale molecular dynamics simulations, kinetic theory, and fluid mechanics.

Accomplishment—Theory: We have demonstrated that a basic kinetic theory of granular gases, the Maxwell model, is analytically tractable. We have found that dissipation strongly affects the velocity distributions, and that velocity correlations generally develop due to the inelastic collisions. Generally, the velocity distributions are non-Maxwellian. We have obtained analytical results for gases constituting of identical particles, polydisperse particles, mixtures, and impurities.

Simulation: We have developed an event-driven molecular dynamics simulation capable of simulating 10^6 particles colliding more 10^{11} collisions overall. This simulation, one of the largest granular materials simulations, allows us to find that the asymptotic dynamics of freely cooling gases are universal, and that it differs from the predictions of current hydrodynamics models. We have also shown that although strong correlations, clustering (Fig.1), and singularities occur, there is a well-defined velocity field.

Significance—The theoretical results are the first exact analytic solutions in the kinetic theory of granular gases. They demonstrate the fundamental difference between granular gases and molecular gases. These results are currently being extended by several research groups across the world. The simulation results resolve outstanding issues concerning clustering and velocity statistics in freely evolving granular gases. They also provide a connection between granular gases and hydrodynamic theory of the formation of large-scale structure in the universe.
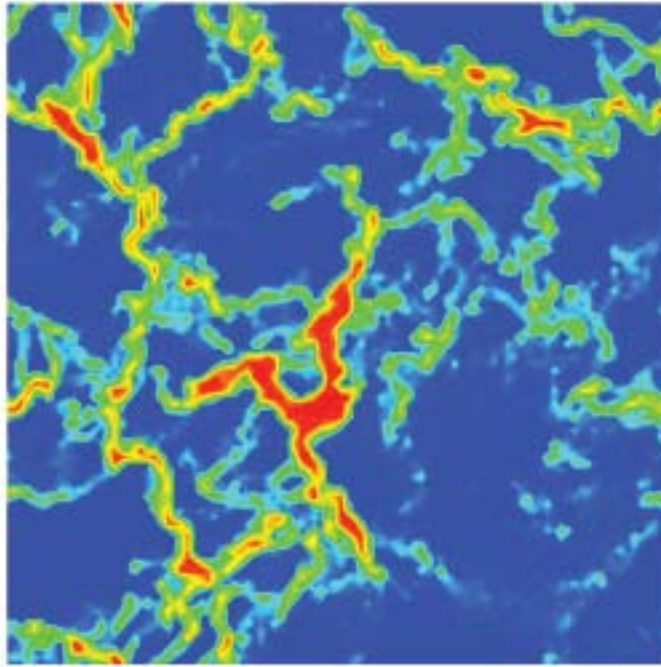
Contact: Eli Ben-Naim, Los Alamos National Laboratory
Phone: (505) 667-9471, Fax: (505) 665-3003, E-mail: ebn@lanl.gov

Figure 1. Formation of large-scale density inhomogeneities in freely evolving granular gas.

Packings of Granular Particles

Gary S. Grest, James W. Landry, and *Steve J. Plimpton,* *Sandia National Laboratories, NM*
Leonardo E Silbert, *University of Chicago*

Motivation—The formation and nature of the structure of granular packings has been a long-standing problem of interest in both the physics and engineering communities. One practical problem is to characterize the stresses generated by granular materials on the walls of silos and thus prevent silo failure. Unfortunately there is no consensus of the correct continuum model for the stress build up in a silo and most of the particulate level simulations have been in two dimensions. Much of the analysis of stresses in a silo is based on the pioneering 1895 theoretical work of Janssen. This analysis is based on several approximations, which have not been thoroughly tested due to the difficulty in performing experiments on the forces between particles and between particles and the silo walls. Particulate level simulations in three dimensions are ideally suited to investigate this problem.

Accomplishment—To understand the internal structure and stresses in a silo, we carried out a systematic simulation study of the effect of various parameters on granular packings using our highly parallel molecular dynamics code. We prepared static granular packings in silos in a variety of ways, including pouring as shown in Figure 1 and particle sedimentation in the presence of a background fluid. We studied the dependence of the stress on method of construction and on the coefficient of friction μ between particles and between particles and the wall.

In liquids, hydrostatic pressure increases with depth, while in granular materials the pressure is independent of depth for piles deeper than about 6R, where R is the radius of the silo as shown in Figure 2. This occurs because granular materials can support shear so that the side walls of a container can support some of the load. Janssen's original analysis assumes that granular packings can be treated as a continuum medium in which vertical stress applied to a material automatically generates a horizontal stress. A second assumption is that the frictional forces between particles and the wall are always at the point of Coulomb failure, where the frictional forces can no longer resist tangential motion of the particles. We find that these assumptions are not strictly correct, particularly the latter - not all particles at the wall are at the maximum tangential load. This leads to a reduction in the effectiveness of the walls to support the load of the particles. In addition, there is an unexplained hydrostatic-like region at the top of the pile where the stress increases linearly with depth. This region, though not predicted by the Janssen analysis, has also been seen in some recent experiments.

Significance—With our new highly parallel algorithm, we are able to study a wide variety of problems in granular ceramics. We can model large systems and obtain precise information in the bulk of a granular system, which cannot be obtained experimentally. These simulations can give valuable guidance in developing constitutive relations and in determining the physical constants necessary to enable finite element analysis of manufacturing processes, such as forming of advanced ceramics. Here we presented an example of pouring particles into a cylindrical container or silo, although we have also studied more complex geometries as would be found in a ceramic die. Future work will focus on understanding the packing of polydispersed materials and discharge from a hopper, particularly on the internal stress distribution during flow.

Contact: Gary S. Grest, Sandia National Laboratories, NM
Phone: (505) 844-3261, Fax: (505) 844-9781, E-mail: gsgrest@sandia.gov
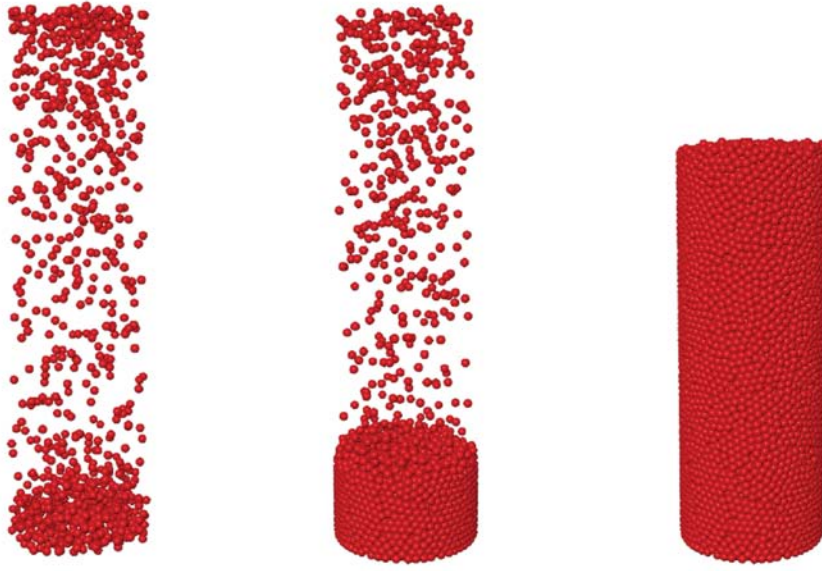
Figure 1. Formation of a granular packing consisting of 20,000 spheres in a cylindrical container of radius R=10d, where d is diameter of the particles. The packing is constructed by pouring particles from a height of 70d. Three configurations of early, intermediate and late times are shown.
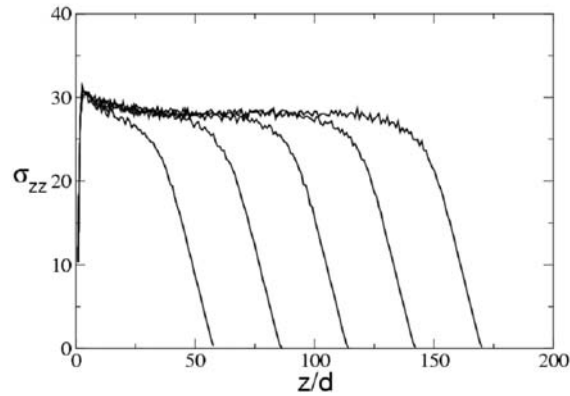

Figure 2. Vertical stress (units of mg/d_2) for packings of 20,000 to 60,000 particles for R=10d. Note the hydrostatic-like linear region near the top of the pile and the height independent stress for piles deeper than approximately 6 times the radii.

Velocity Fluctuations in Electrostatically Driven Granular Monolayers

I. S. Aronson, Argonne National Laboratory
J. S. Olafsen, University of Kansas

Motivation—Despite extensive study over the preceding decade, a fundamental understanding of the dynamics of granular materials still poses a challenge for physicists and engineers. Driven granular materials exhibit complex behavior that resemble some aspects of conventional solids, liquids, and gases, yet also demonstrate some considerable differences. A key distinction that separates granular phases from their conventional counterparts is the presence of dissipation of energy through inelasticity of collisions and friction. Recent experimental studies with vibrationally-driven granular gases revealed surprising deviations in the particle distribution function from the Maxwell distribution law. These deviations were attributed to the effects of dissipation due to inelasticity of inter-particle collisions. In particular a "universal" stretched exponential law with the exponent $\zeta=3/2$ was reported. This behavior was observed in a wide range of frequencies and amplitudes of vibration and for different densities of the granular gas. These studies suggest that the deviations from a Maxwell distribution are the result of short-range inelastic hard-core collisions between particles. However, interactions between particles often are not reduced to simple hard-core collisions. An important question is whether non-Maxwellian distributions are typical only for granular gases with hard-core collisions or could non-Maxwellian distributions also be observed for general dissipative gases with both short-range and long-range interactions.

Accomplishment—We have studied the particle velocity distributions in electrostatically-driven granular media. We have found that in a wide range of parameters the particle velocity distribution function is strongly non-Maxwellian and is well-approximated by the stretched exponential law , where v_0 is thermal velocity. We performed molecular dynamics simulations of conducting particles in an ac electric field and have obtained qualitative agreement with the experiment. We conclude from our results that the tails of the velocity distributions for driven granular gases, in general, exhibit non-Maxwellian behavior and are not limited to the systems with just hard-core collisions. Our experimental $P(v) \sim \exp[-|v/v_0|^{3/2}]$ setup is shown in Figure 1. Particles are placed between the plates of a large capacitor which is energized by a constant (dc) or alternating (ac) electric field $E=E_0 \cos(\omega t)$. To provide optical access to the cell, the capacitor plates were made of glass with a clear conductive coating. We used 11x11 cm capacitor plates with a spacing of 1.5 mm. The particles consisted of 165 µm conducting bronze spheres. Particle trajectories were acquired by high-speed videomicroscopy. Selected experimental results are presented in Figures 2 and 3. Figure 2 illustrates the effects of long-range interactions on inter-particle collisions. Figure 3 presents typical horizontal velocity distribution in our electrostatic cell. We have found stretched exponential velocity distributions in the wide range of experimental conditions.

Significance—Electrostatic driving makes use of *bulk* forces, and allows control of the ratio between long-range electric forces and short-range collisions by changing the amplitude and the frequency of the applied electric field. We have found that in a wide range of experimental parameters the particle velocity distribution function is strongly non-Maxwellian, evidence that short-range forces contribute to non-Gaussian distributions may have relevance for completely different systems, such as dusty plasmas and charged colloids.

Contact: Igor Aronson, Argonne National Laboratory
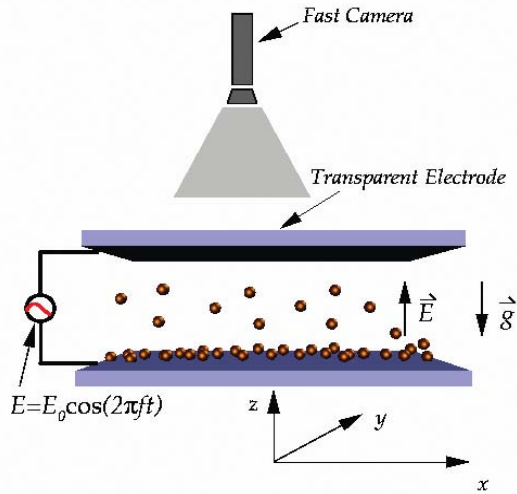Phone: (630) 252-9725, Fax: (630) 252-7777, E-mail: aronson@msd.anl.gov

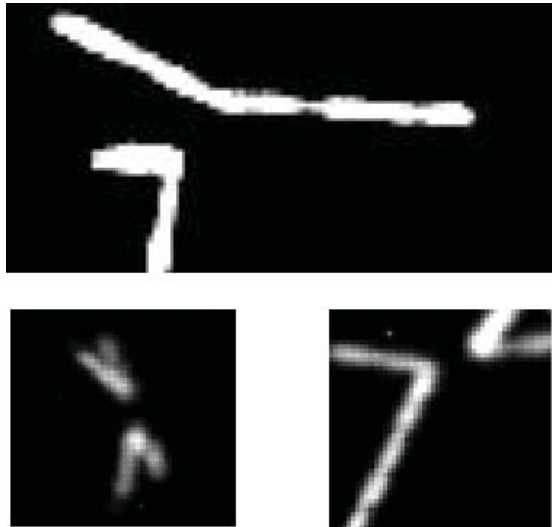Figure 1. Block-diagram of experimental apparatus.

Figure 2. Composite images of two particles colliding created by overlaying several sequential images taken with the high-speed camera for a driving frequency of 50 Hz. Each of the three images demonstrates a different collision between two particles that occurs at a distance larger than a ball diameter. At this relatively high frequency the particles have a small vertical excursion and the focal plane of the microscope is set between the two plates of the cell. The particles are completely illuminated which results in the smudged streaks of varying intensity in the particle tracks.
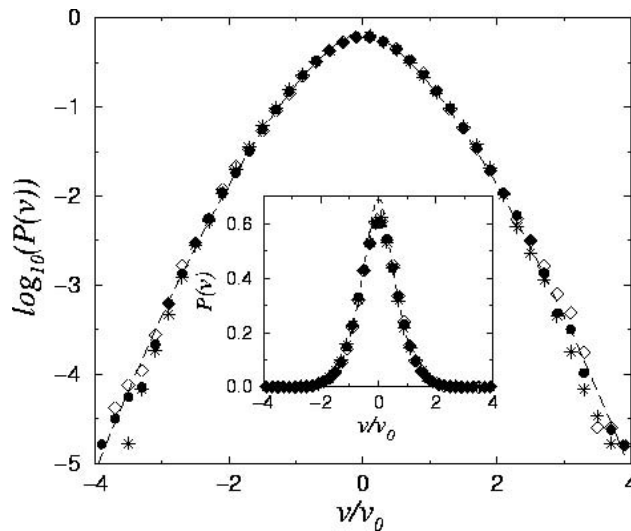

Figure 3. Main plot: The logarithms of horizontal velocity distribution P(v) vs. normalized velocity v/v_0, where v_0 is horizontal "thermal velocity". Bullets correspond to $f=50$ Hz and $E_0=8.83$ kV/cm, stars to $f=120$ Hz and $E_0=8.83$ kV/cm, diamonds to $f=45$ Hz and kV $E_0=7.3$ kV/cm. Dashed line show the best fit to the stretched exponential law with $\zeta \sim 1.51$. Inset: The horizontal velocity distribution P(v) vs. normalized velocity v/v_0 in linear scale.

ABO$_3$ [100]

AO [110]

silicide

Si [110]
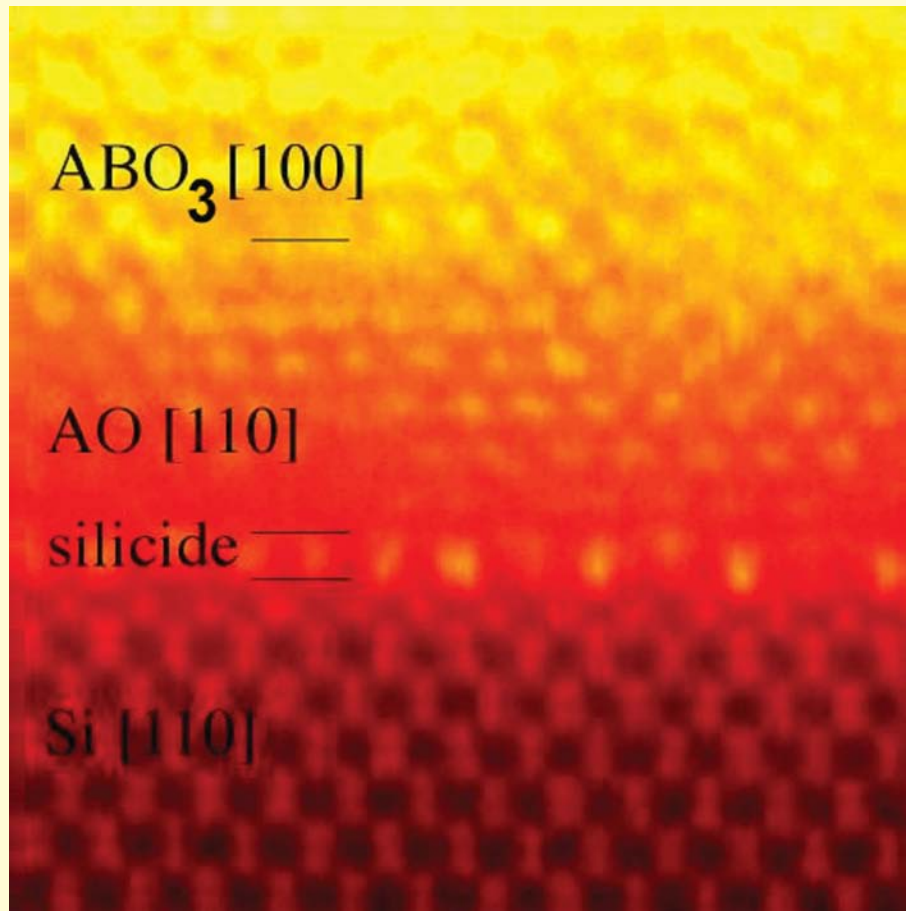
The figures on the front and back covers relate to two of the accomplishments described in this issue of *Research Briefs*. The figure on the front shows the formation of large-scale density inhomogeneities in freely evolving granular gas revealed from kinetic theorgy simulations. The above figure is a Z-contrast image showing the chemical and structured arrangement associated with chemical bonding and epitaxy at the interface between an alkaline earth oxide and silicon.